Phase change, surface tension and turbulence in real fluids

by

Daniel Albernaz

Phase change, surface tension and turbulence in real fluids

Daniel L. Albernaz
Linné FLOW Centre, KTH Mechanics, The Royal Institute of Technology
SE-100 44 Stockholm, Sweden

Abstract

Sprays are extensively used in industry, especially for fuels in internal combustion and gas turbine engines. An optimal fuel/air mixture prior to combustion is desired for these applications, leading to greater efficiency and minimal levels of emissions. The optimization depends on details regarding the different breakups, evaporation and mixing processes. Besides, one should take into consideration that these different steps depend on physical properties of the gas and fuel, such as density, viscosity, heat conductivity and surface tension.

In this thesis the phase change and surface tension of a droplet for different flow conditions are studied by means of numerical simulations. This work is part of a larger effort aiming to developing models for sprays in turbulent flows. We are especially interested in the atomization regime, where the liquid breakup causes the formation of droplet sizes much smaller than the jet diameter. The behavior of these small droplets is important to shed more light on how to achieve the homogeneity of the gas-fuel mixture as well as that it directly contributes to the development of large-eddy simulation (LES) models.

The numerical approach is a challenging process as one must take into account the transport of heat, mass and momentum for a multiphase flow. We choose a lattice Boltzmann method (LBM) due to its convenient mesoscopic nature to simulate interfacial flows. A non-ideal equation of state is used to control the phase change according to local thermodynamic properties. We analyze the droplet and surrounding vapor for a hydrocarbon fuel close to the critical point. Under forced convection, the droplet evaporation rate is seen to depend on the vapor temperature and Reynolds number, where oscillatory flows can be observed. Marangoni forces are also present and drive the droplet internal circulation once the temperature difference at the droplet surface becomes significant. In isotropic turbulence, the vapor phase shows increasing fluctuations of the thermodynamic variables once the fluid approaches the critical point. The droplet dynamics is also investigated under turbulent conditions, where the presence of coherent structures with strong shear layers affects the mass transfer between the liquid-vapor flow, showing also a correlation with the droplet deformation. Here, the surface tension and droplet size play a major role and are analyzed in detail.

Descriptors: Evaporation, equation of state, hydrocarbon fuel, lattice Boltzmann, deformation, droplet heating, critical point, Marangoni forces

Fasövergång, ytspänning och turbulens i icke-ideala fluider

Daniel L. Albernaz
Linné FLOW Centre, KTH Mekanik, Kungliga Tekniska Högskolan
SE-100 44 Stockholm, Sverige

Sammanfattning

Sprayer används i stor utsträckning inom industri, särskilt för bränslen i förbrännings- och gasturbinmotorer. En optimal bränsle/luft blandning före förbränning är önskvärd för dessa tillämpningar, vilket leder till stor effektivitet och minimala nivåer av utsläpp. Optimeringen beror på detaljer angående olika uppbrott, avdunstning och blandningsprocesser. Dessutom bör man beaktas att dessa olika stegen är beroende av fysikaliska egenskaper hos gas och bränsle, såsom densitet, viskositet, värmeledningsförmåga och ytspänning.

I den här avhandlingen kommer fasövergång och ytspänning hos en droppe i olika flödestillstånd att studeras genom numeriska simuleringar. Detta arbete är en del av ett större projekt som siktar till att utveckla modeller för sprayer i turbulenta flöden, vilket har betydelse för energiomvandling av bränslen. Vi är särskilt intresserade av atomiseringsregimen, där vätskan vid uppbrottet bildar droppstorlekar mycket mindre än stråldiametern. Beteendet hos dessa små droppar är viktigt för att tillföra ytterligare klarhet över hur man kan uppnå homogenitet i gas-bränsleblandningen, såväl som den bidrar direkt till utvecklingen av large-eddy simulation (LES) modeller.

Den numeriska metoden är en utmanande process där man måste beakta transport av värme, massa och rörelsemängd för en flerfasströmning. Vi väljer en Lattice Boltzmann Method (LBM) på grund av dess mesoskopiska natur att simulera strömning med fria gränsytor. En icke-ideal tillståndsekvation används för att styra fasomvandling baserat på lokala termodynamiska egenskaper. Vi undersöker droppen och kringliggande ånga för ett kolvätebränsle nära den kritiska punkten. Under påtvingad konvektion synes en droppes förångningshastighet bero på ångtemperaturen och Reynolds tal, och oscillerande flöden kan observeras. Marangoni-krafter är också närvarande och driver på droppens inre cirkulation när temperaturskillnaden vid droppytan blir betydande. I isotrop turbulens visar ångfasen ökande fluktuationer i de termodynamiska variablerna när fluiden närmar sig den kritiska punkten. Droppdynamik undersöks också i turbulens, där förekomsten av sammanhängande strukturer med starka skjuvskikt påverkar massöverföringen mellan vätske och ånga, som också visar en korrelation med droppens deformation. Ytspänning och droppstorlek har stort inflytande och analyseras i detalj.

Nyckelord: Avdunstning, tillståndsekvation, kolvätebränsle, lattice Boltzmann, deformation, droppe uppvärmning, kritisk punkt, Marangoni-krafter

Preface

This thesis contains numerical investigations of phase change and surface tension of a droplet for different flow conditions. Turbulent effects in single and multiphase cases are also considered. The thesis is divided in two parts, where the first one presents an overview of the work and the main results. The second part consists of five journal articles. The layout of these papers has been adjusted to fit the format of this thesis, but their content has not been changed with respect to the original versions.

Paper 1.
ALBERNAZ, D. L., DO-QUANG, M. & AMBERG, G., 2013 Lattice Boltzmann Method for the evaporation of a suspended droplet. *Interfac. Phenom. Heat Transfer* **1**, 245-258

Paper 2.
ALBERNAZ, D. L., DO-QUANG, M. & AMBERG, G., 2015 Multirelaxation-time lattice Boltzmann model for droplet heating and evaporation under forced convection. *Phys. Rev. E* **91**, 043012

Paper 3.
ALBERNAZ, D. L., AMBERG, G. & DO-QUANG, M., 2016 Simulation of a suspended droplet under evaporation with Marangoni effects. *Accepted for publication in Int. J. Heat Mass Transfer*

Paper 4.
ALBERNAZ, D. L., DO-QUANG, M., HERMANSON, J. C. & AMBERG, G., 2016 Real fluids near the critical point in isotropic turbulence. *Under revision for publication in Phys. Fluids*

Paper 5.
ALBERNAZ, D. L., DO-QUANG, M., HERMANSON, J. C. & AMBERG, G., 2016 Droplet deformation and heat transfer in isotropic turbulence. *Submitted to J. Fluid Mech.*

Division of work between authors

The main advisor of the project is Prof. Gustav Amberg (GA) and the co-advisor is Dr. Minh Do-Quang (MDQ).

Paper 1

The code was developed and implemented by Daniel Albernaz (DA). Simulations and analysis were carried out by DA. The paper was written by DA with feedback from GA and MDQ.

Paper 2

Implementations amd modifications were done by DA and MDQ, where the code Palabos was used. DA performed the computations and analyzed the data. The paper was written by DA with feedback from GA and MDQ.

Paper 3

Implementations on the code, simulations and analysis were carried out by DA. The paper was written by DA with feedback from GA and MDQ.

Paper 4

Modifications on the code were carried out by DA with help of MDQ. The computations and analysis were performed by DA. The paper was written by DA with feedback from GA and MDQ. Prof. Jim Hermanson (JH) was also involved in discussions and provided feedback on the paper.

Paper 5

Modifications on the code were carried out by DA. Simulations and analysis were done by DA. The paper was written by DA with feedback from GA, MDQ and JH.

Part of the work has been presented at the following international conferences:

Albernaz, D. L., Do-Quang, M. & Amberg, G.
Convective effects on evaporating droplet with the lattice Boltzmann method.
11th International Conference for Mesoscopic Methods in Engineering and Science (ICMMES) – New York, USA, 2014

Albernaz, D. L., Do-Quang, M. & Amberg, G.
Droplet dynamics in homogeneous isotropic turbulence. 68th Annual Meeting of the APS Division of Fluid Dynamics – Boston, USA, 2015

x

If you're not failing every now and again, it's a sign you're not doing anything very innovative.

Woody Allen, 1935–

Contents

Part I

Overview & Summary

CHAPTER 1

Introduction

The richness of fluid dynamics can be easily observed as we turn on the tap in the bathroom. There are several interesting physical aspects to look into as the water stream interacts with the surrounding air and splashes into the sink. The gravity and velocity inlet play a major role in this scenario: as we increase the water flow rate, instabilities are introduced and a breakup of the liquid jet is observed, as seen in Fig. 1.1. The result is the formation of ligaments and smaller drops, which contribute to increase the complexity of such flow.

FIGURE 1.1. (left) The water stream from a tap with high flow rate; (right) the formation of ligaments and droplets due to the breakup of the liquid jet.

To make it even more complicated, we could modify the conditions of the surrounding air. Let us consider a gas with higher temperature and pressure than the liquid fluid, where the difference between thermodynamic properties would generate phase change. We could also change the location from the bathroom to a combustion chamber where liquid fuel flows from narrow nozzles instead. We are now dealing with an energy conversion system such as an internal combustion engine or a gas turbine, which are essential to modern human life. Similar to the tap water case, a fuel jet at high flow rate would show an initial breakup that implies forming smaller structures as liquid sheets, ligaments and droplets.

1.1. Fuel sprays: state of the art

The conventional understanding of spray formation when liquid leaves the nozzle is based on the separation of the following stages (Lefebvre (1989)): development of a jet, conversion of a jet into liquid sheets and ligaments, disintegration of ligaments into relatively large droplets (primary breakup) and breakup of large droplets into smaller ones (secondary breakup). The liquid jet may break up into drops of widely different diameters, with sizes varying from the nozzle diameter down to droplets of diameters several orders of magnitude smaller. The size distribution is in general not uniform and depends on local flow conditions and properties of the fuel and gas.

Different dimensionless numbers can help describing the flow and breakup processes, among them the Reynolds number Re, which gives the ratio between the inertial and viscous forces, and Weber number We that consists of the ratio of inertia to surface tension force. Figure 1.2 shows a classical breakup regime given by a phase diagram between Re and We. The instability of a heavy fluid layer supported by a light one is known as Rayleigh instability and occurs under an acceleration of the fluid system in the direction toward the denser fluid (Rayleigh (1883)). This kind of instability is mainly observed in the phase diagram when $Re < 10^3$ and $We < 1$. By increasing Re and/or We by one order of magnitude, the jet becomes wavy due to aerodynamic effects, known as the non-axisymmetric Rayleigh breakup. When Re is further increased, the shear stresses at the gas/liquid interface strip off droplets. For a given combination of Re and We a regime known as membrane breakup can be obtained, where the whole round jet forms a thin sheet (membrane) before breaking into drops. When even larger Reynolds numbers are used, $Re \sim 10^5$, short-wavelength shear instability takes place, known as atomization regime. Here, the disintegration process begins at the jet surface and gradually erodes the jet until it is completely broken up, as seen in Fig. 1.3[1]. Droplet sizes much smaller than the jet diameter can be observed. Atomization is achieved beyond the upper bound of membrane breakup as seen in Fig. 1.2, and the farther away from the bound, the finer the spray.

Experiments dealing with breakup of liquid jets are difficult due to the large number of droplets. When non-intrusive methods are used, the light is scattered by the presence of these particles, making the spray opaque. Therefore, most of the available data is related to the average temporal development of the spray by high-speed imaging or shadowgraphs (Dec (1997)). Regarding turbulent mixing, which can be measured by Laser Induced Fluorescence (LIF) as seen in Guillard *et al.* (1998), its combination with Particle Image Velocimetry (PIV) allows the simultaneous measurement of concentration and velocity field.

---

[1]Lasheras, J. C., Villermaux, E. & Hopfinger, E. J. 1998 Break-up and atomization of a round water jet by a high-speed annular air jet. *J. Fluid. Mech.* **357**, 351–379, Fig. 2 (g) ©Cambridge University Press.
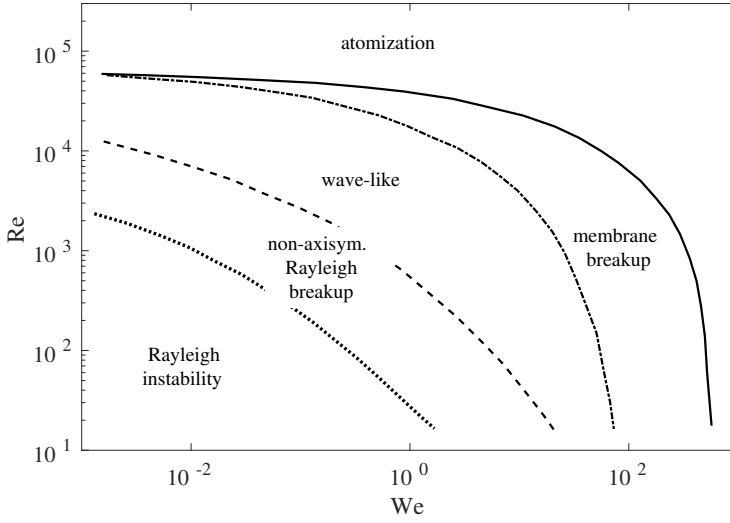
FIGURE 1.2. Breakup regimes of a jet given for a $Re - We$ diagram.
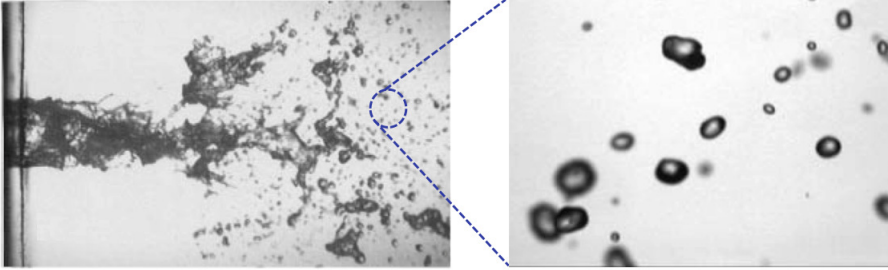
FIGURE 1.3. Representation of a fuel liquid jet atomization for high Re number (left), where the formation of ligaments and droplets much smaller than the jet diameter (right) are observed.

By combining these methods one is able to directly measure the turbulent fluxes of the fluid under consideration (Borg *et al.* (2001)). The recent introduction of high speed shutters (Sedarsky *et al.* (2007)) allows the capturing of individual droplets and filaments in the spray cloud. However, this method is still under development and requires special equipment. Much still has to be done in order to obtain experimental data for the wide range of scales that characterize a spray with high Re number.

When simulating atomization of liquid jets, the dominant method in industrial applications consists of the Reynolds-averaged Navier-Stokes (RANS). In this method, drastic simplifications are made, where physical modelling of atomization and sprays is an essential part of the two-phase flow computation (Gorokhovski & Herrmann (2007)). Parameter tuning is usually necessary with reference experimental data, and this should be done every time when the flow conditions are changed. In more advanced cases such as direct numerical simulation (DNS) and large-eddy simulation (LES), physical modelling of atomization and jets is still inevitable (Jiang *et al.* (2010)). For multiphase flows, there is no model-free DNS since the interactions between different phases need to be described. Even though detailed DNS with high resolution simulations have been performed (e.g. Shinjo & Umemura (2010) and Shinjo & Umemura (2011)), there are also assumptions regarding surface tension forces and/or temperature for droplets in the smallest scales.

Overall, fuel sprays are extensively applied in industry, where an optimal fuel/air mixture prior to combustion is desired, leading to best efficiency and minimal levels of emissions (Shi *et al.* (2011)). In order to optimize fuel sprays, details regarding the different breakups, evaporation and mixing processes should be scrutinized and well understood. Besides, one should take into account that these processes depend on physical properties of the gas and fuel, e.g. density, viscosity, heat conductivity and surface tension.

Recently, different research groups at KTH Mechanics started a collaborative project aiming for developing simulations and models for droplets clouds and sprays in turbulent fluid flows, with relevance for energy conversion of mixtures of biofuels and conventional fuels. The project was divided into four branches: *(i)* the LES modelling of secondary droplet breakup and turbulent mixing process, as seen in Fig. 1.4 [2], with the goal of understanding the interaction between turbulence characteristics and the droplet physical properties; *(ii)* the different breakup processes of liquid sheet and droplets under different flow conditions by using a Volume of Fluid (VOF) approach (Kékesi *et al.* (2014)); *(iii)* development of subgrid-scale models for LES of reacting and turbulent flows by using new modelling concepts (Grigoriev *et al.* (2013)); *(iv)* DNS of droplets under evaporation in idealized conditions, where surface forces may dominate. The last part is to be handled by a diffuse interface method in microscopic dimensions and is the context of the present thesis. The parts *(ii)*, *(iii)* and *(iv)* would provide information for the development of LES models that could be used in part *(i)*.

---

[2]Nygård, A. & Fuchs, L. 2013 Numerical investigation of mixing in intermittent jets. *14*th *European Turbulence Conference.*
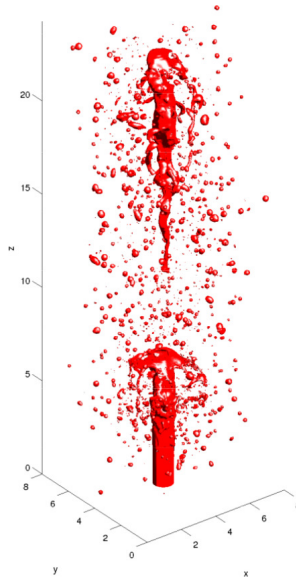
FIGURE 1.4. Illustration of a LES simulation for an incompressible liquid turbulent jet break-up.

1.2. Scope of the thesis

As we draw attention to the smaller scales in a fuel spray under an atomization regime, droplets between $\approx 0.2mm$ to nanoscales can be observed. These small droplets are more sensitive to local temperatures as they have larger surface area to volume ratio in comparison to larger ones. In other words, smaller droplets are heated up more quickly, which makes the evaporation process faster. The evaporation rate would depend on the flow condition and local thermodynamic properties. These droplets are also responsive to a turbulent environment: it is expected that the presence of coherent structures with strong shear layers should affect the mass transfer between the liquid-vapor flows, where surface tension might also play an important role under certain conditions. The droplet behavior may shed more light on how to achieve the homogeneity of the mixture of the fuel and the surrounding air.

The primary focus of this work is to numerically investigate the dynamics of a single droplet in different flow conditions, where surface tension, phase change and turbulent effects are analyzed in detail. This is an important step to gain in-depth insight into the different physical phenomena taking place inside a fuel jet. Moreover, it contributes directly for modelling the smaller scales present in fuel sprays, which consists in one of the goals from the collaborative project between different research groups at KTH Mechanics. Although the study of a single droplet dynamics may sound simple, the numerical approach is a challenging process as one must take into account the transport of heat, mass

and momentum for a multiphase flow. We make use of a lattice Boltzmann method, shown as a promising method for dealing with interfacial flows as it can address macro- and microscales. A non-ideal equation of state is used to control the phase change according to local thermodynamic properties, where a hydrocarbon fuel is taken into consideration. In order to obtain a density ratio as observed in Diesel engines under operational conditions (between 20 and 65, as seen in Taylor (1985)), we analyze the droplet and surrounding vapor close to the critical point.

The following chapters present the relevant theoretical and physical aspects contained in this thesis. Chapter 2 describes the phase change, where the latent heat and different equations of state are discussed. The theoretical droplet heating and evaporation is also derived for a static condition. Chapter 3 introduces the surface tension and the Marangoni effect. Chapter 4 gives a brief description of turbulence. Chapter 5 provides an overview of the numerical method used. We summarize the main results in Chapter 6 and present concluding remarks in Chapter 7.

CHAPTER 2

Phase change

A transition from one state of matter (solid or liquid or gas) to another without
a change in chemical composition is defined as phase change. During this
transition, a system either absorbs or releases a fixed amount of energy per
volume, changing the arrangement of the molecules as seen in Fig. 2.1. The
temperature of the system stays constant as heat is added or taken from the
process. The amount of heat q can be expressed as the product of the mass m
and the specific latent heat L of the material, following

$$q = mL \ . \tag{2.1}$$

The specific latent heat measures the change in enthalpy during the phase
change taken at constant temperature. In the case of phase transition from
liquid to vapor, the difference between the vapor and liquid enthalpies gives
the latent heat of vaporization L_{hv}, written as

$$L_{hv} = \Delta h = h_v - h_\ell \ , \tag{2.2}$$

where h is enthalpy and the subscripts v and ℓ denote the vapor and liquid,
respectively. In evaporation, the energy added is used to break the bonds
between the molecules. For a pure substance, liquid-vapor phase change always
occurs at the saturation temperature. Since the phase change in our numerical
model is controlled by an equation of state, some basic concepts are described
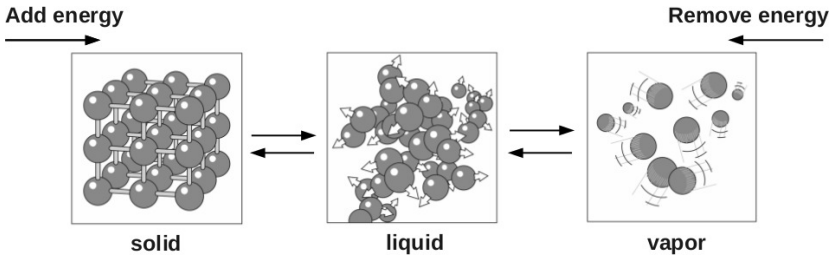below.

FIGURE 2.1. Phase change between the states of matter, where
different arrangement of molecules are obtained.

2.1. Equations of state

The expression *equation of state* (EOS) refers to equilibrium relationships involving pressure p, temperature T and specific volume v (which can also be written in terms of density ρ, where $v = 1/\rho$). If the vapor or gas can be approximated as an ideal gas, the EOS is given as

$$pv = RT \ , \qquad (2.3)$$

where R is the gas constant. It is known that an ideal EOS is inaccurate in describing the behavior of many fluids, especially as critical point or saturation conditions are approached. In addition, an ideal gas EOS is of course incapable of modelling the liquid phase. A non-linear cubic EOS includes the interaction between molecules and takes into account a finite molecule volume. These considerations deviate from ideality and allow a non-ideal EOS to describe several fluids with good agreement, especially their liquid-vapor properties close to the critical point. The van der Waals (vdW) EOS is the simplest and most well-known cubic EOS, given by

$$p = \frac{RT}{v - b} - \frac{a}{v^2} \ , \qquad (2.4)$$

where $a = 27(RT_c)^2/(64p_c)$ is the attraction parameter and $b = RT_c/(8p_c)$ represents the volume occupied by the molecules of the substance, i.e. the repulsion parameter. The subscript c denotes the variable value at the critical point. Different non-ideal EOS have been proposed in an effort to improve the EOS accuracy. Kaplun & Meshalkin (2003) proposed the M-K EOS which has the following form

$$p = \frac{RT}{v} \left(1 + \frac{c'}{v - b'} \right) - \frac{a'}{v^2} \ , \qquad (2.5)$$

where a', b' and c' are parameters used to fit the desired experimental data. Note that for $b' = c'$, the vdW EOS is obtained. Another renowned EOS is the Peng-Robinson P-R EOS, given by

$$p = \frac{RT}{v - b} - \frac{a\alpha'(T)}{v^2 + 2bv - b^2} \ , \qquad (2.6)$$

with $a = 0.45724R^2T_c^2/p_c$ and $b = 0.0778RT_c/p_c$. The parameter $\alpha'(T) = [1 + (0.37464 + 1.54226w - 0.26992w^2)(1 - \sqrt{T/T_c})]^2$ is defined according to the acentric factor w and is a function of the actual temperature T. An EOS is useful for predicting the $p - v - T$ behavior of a fluid in a desired range of values. A $T - v$ diagram can be used for finding the coexisting specific volumes of the liquid and vapor phases as a function of temperature. A curve in this diagram represents the saturated liquid and vapor lines.

In order to find the specific volumes analytically, a Maxwell construction could be used (Faghri & Zhang (2006)). The Maxwell construction, also known

as the "equal area rule", is derived from the condition that the free energies of the gas and the liquid must be equal when they coexist. The $T - \upsilon$ diagram of the fluid chosen for performing numerical simulations can be obtained by experimental data. The comparison of the data to the Maxwell construction for a specific EOS is a way to evaluate if such EOS is suitable for representing the desired fluid. Hydrocarbon fluids are common fuels when one has in mind the application of evaporating fuel in different engines. Throughout this thesis we make use of a hexane fluid (C_6H_{14}), where the respective real values are obtained from Lemmon *et al.* (2013). The acentric factor of hexane is $w = 0.30075$.

Figure 2.2 shows the reduced temperature T_r as a function of the reduced specific volume, υ_r. Thermodynamic variables are shown in terms of the reduced variables, i.e. the actual quantity normalized by the critical value. Therefore, the critical point corresponds to $T_r = 1$ and $\upsilon_r = 1$. The experimental data is plotted with the analytical solutions of different EOS. When compared to a nonpolar heavy hydrocarbon such as hexane, the vdW EOS presents poor agreement both for the liquid and vapor phases. The M-K EOS shows better results, however errors of the order of $\sim 90\%$ for the liquid phase far from the critical point ($T_r \approx 0.7$) are present. The P-R EOS shows good agreement with the experimental data, especially for the vapor phase, where error is maintained below 1%. We adopt the P-R EOS through the rest of this thesis. We would like to mention that the coexistence curve from numerical simulations matches the analytical solution of the P-R EOS (Albernaz *et al.* (2015)).
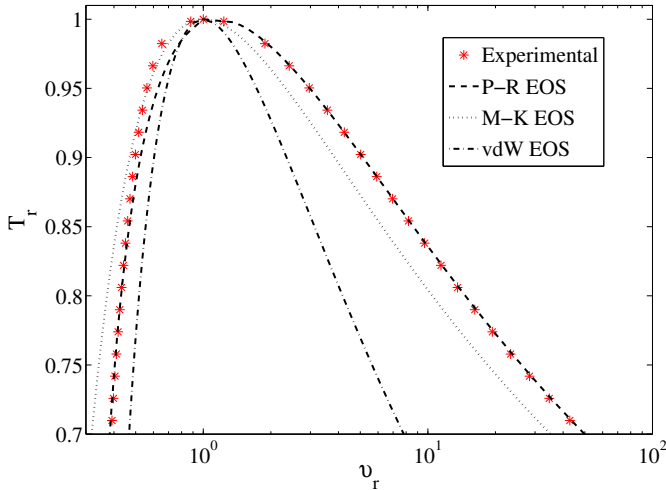

FIGURE 2.2. Reduced temperature T_r as a function of the reduced specific volume υ_r, for different equations of state, where a hexane fluid (C_6H_{14}) is considered. Taken from Albernaz *et al.* (2013).

2.2. Clausius-Clapeyron relation

An equilibrium state for two phases of a pure substance (single component) is given when both have the same temperature and pressure. If the temperature of a two-phase system in equilibrium is changed slightly, the pressure of the system will be affected; this relationship is described by the Clausius-Clapeyron relation (Faghri & Zhang (2006)). On a pressure-temperature $P - T$ diagram one can also obtain the coexistence condition, which is characterized by a curve that separates one phase from the other. The Clausius-Clapeyron relation gives the slope of the tangents to this curve, and is written as

$$\frac{dP}{dT} = \frac{\Delta s}{\Delta v} \ ,$$
(2.7)

where dP/dT is the slope of the tangent to the coexistence curve at any point, Δs and Δv are the change in specific entropy and specific volume, respectively. The entropy change can be defined as the enthalpy variation divided by the thermodynamic temperature $\Delta s = \Delta h/T$. By using Eq. (2.2), entropy change is rewritten as

$$\Delta s = \frac{L_{hv}}{T} \ .$$
(2.8)

The latent heat of vaporization can be explicitly expressed by combining the definition in Eq. (2.8) with Eq. (2.7), obtaining

$$L_{hv} = T\frac{dP}{dT}(v_v - v_\ell) \ .$$
(2.9)

Using the P-R EOS in Eq. (2.6) and for a certain temperature, the latent heat of vaporization in our model can be evaluated through the RHS of Eq. (2.9). The latent heat data obtained from Lemmon *et al.* (2013) matches with the one obtained in the model used.

2.3. The D^2 law

The evaporation of a liquid fuel consists of the detachment of molecules from its surface, where there is diffusion of the vapor formed into the surrounding environment. In order to model the evaporation, some assumptions can be made: one can consider a motionless and isolated pure liquid droplet, where the surrounding medium is inert and has a uniform higher temperature than the droplet to trigger the phase change. The droplet shape is considered spherical and slow evaporation (quasi-steady assumption) is utilized. The one-component equation of transport of heat in spherical coordinates is given by:

$$r^2\rho c_p \mathrm{v}_r \frac{\partial T}{\partial r} = \frac{\partial}{\partial r}\left(r^2 k \frac{\partial T}{\partial r}\right) \ ,$$
(2.10)

where r is the radial distance from the droplet center, v_r is the velocity in the radial direction and k is the thermal conductivity. The term c_p represents the specific volume at constant pressure, which is assumed constant as the slow evaporation has the implication of considering a limited temperature difference between the phases. It is important to note that in one-component evaporation the equation of transport of heat is sufficient due to the presence of only self-diffusion, i.e. the vapor is diffused into the surrounding vapor (Holyst *et al.* (2013)). The mass balance at the interface requires that the steady state vapor flux equals the evaporation rate at the droplet. Therefore, the continuity equation is given as

$$r^2 \rho v_r = r_i^2 \rho_i v_i \; . \tag{2.11}$$

By using Eq. (2.11) we integrate Eq. (2.10) with respect to r, which gives

$$r_i^2 \rho_i v_i c_p \frac{\partial T}{\partial r} = r^2 k \frac{dT}{dr} + \text{constant} \; , \tag{2.12}$$

where the integration constant is determined from algebraic manipulations, according to the boundary condition given from the energy balance at the interface, which assumes (Sirignano (2010))

$$R^2 k_v \frac{dT}{dr}\bigg|_{i,v} = R^2 k_\ell \frac{dT}{dr}\bigg|_{i,\ell} + R^2 \rho_i v_i L_{hv} = R^2 \rho_i v_i L_{eff} \; , \tag{2.13}$$

where L_{eff} denotes the effective latent heat of vaporization, R is the droplet radius and subscript i refers to quantities evaluated at the interface. The temperature of the entire droplet is generally considered constant, as the transport of heat inside the droplet is negligible, i.e. $L_{eff} = L_{hv}$, which is also assumed in order to obtain an analytical solution. Using the boundary condition in Eq. (2.13), Eq. (2.12) becomes

$$r_i^2 \rho_i v_i c_p \left(T - T_i + \frac{L_{hv}}{c_p} \right) = r^2 k \frac{dT}{dr} \; . \tag{2.14}$$

After separating the variables we integrate Eq. (2.14) within the intervals $[r_i, r_\infty]$ and $[T_i, T_\infty]$, obtaining

$$\frac{r_i^2 \rho_i v_i c_p}{r} = k_i \ln \left(\frac{T_\infty - T_i + L_{hv}/c_p}{T - T_i + L_{hv}/c_p} \right) \; , \tag{2.15}$$

setting r equal to r_i at the surface, we have

$$r_i v_i \rho_i c_p = k_i \ln(1 + B) \; , \tag{2.16}$$

where the nondimensional Spalding number B is given as

$$B = \frac{c_p(T_\infty - T_i)}{L_{hv}} \; . \tag{2.17}$$

Using the mass continuity at the droplet surface $-\rho_\ell dr_i/dt = \rho_i v_i$ and now integrating for r and t, for an initial diameter D_0, the diameter D evolution in time is obtained as

$$D^2 = D_0^2 - \left[\frac{8\alpha_i \rho_i}{\rho_\ell} \ln(1+B) \right] t \; , \tag{2.18}$$

where $\alpha_i = k_i/(c_p \rho_i)$ is the thermal diffusivity evaluated at the interface. Equation (2.18) is known in literature as the D^2 evaporation law (Kuo (2005)), where the evaporation coefficient is given as

$$\beta_v = \frac{8\alpha_i \rho_i}{\rho_\ell} \ln(1+B) \; . \tag{2.19}$$

The evaporation coefficient β_v represents the magnitude of the negative slope of the straight line obtained when D^2 is plotted as a function of time. In this way, the droplet evaporation time (lifetime) can be written as $t_{ev} = D_0^2/\beta_v$, which is seen to be longer for larger droplets. Even though several simplifications were made, the D^2 law has been verified by numerous experimental data. However, it is important to mention that this analytical solution is not valid under many flow conditions and thermodynamic properties.

CHAPTER 3

Surface tension

In a liquid there is an attractive force between molecules that is absent in gases. The surface tension is produced due to this difference between intermolecular forces at the liquid-vapor interface. Even though the interface is often treated as a sharp discontinuity on the macroscale, the change of properties between different phases has a microscopic origin (Faghri & Zhang (2006)).

Near the interphase boundary, the density varies in space, and the interfacial energy can be computed as an excess energy of this inhomogeneous layer. If deformation occurs, both the shape and the area of the surface will affect the internal energy of the interface. Therefore, surface tension is responsible for the shape of liquid droplets.

3.1. The Young-Laplace law

For a liquid droplet suspended in the vapor phase as illustrated in Fig. 3.1 (left), the pressure inside is related to the vapor pressure by the Young-Laplace equation

$$\Delta p = \sigma \left(\frac{1}{R_1} + \frac{1}{R_2} \right) \ , \tag{3.1}$$

where R_1 and R_2 are the droplet radii of curvature in each of the axes that are parallel to the surface and $\Delta p = p_\ell - p_v$ is the pressure difference between the droplet interior and the vapor. The surface tension is denoted as σ. For a spherical droplet, $R_1 = R_2 = R$. The Young-Laplace law can be obtained from the force balance. In a half-sphere droplet, the surface tension force acts parallel to the surface, given as the surface tension times the circumference, $\sigma 2\pi R$. In order to have a droplet in equilibrium, the opposite force due to pressure difference times the area $\Delta p \pi R^2$ has to be of the same magnitude, where the equality becomes Eq. (3.1).

Figure 3.1 (right) shows the verification of the Young-Laplace law done for our numerical model (in lattice units). Different values for the surface tension can be achieved in the model by changing the interface thickness, which is controlled by a dimensionless parameter κ (Márkus & Házi (2011)). The symbols indicate the numerical results whereas solid lines correspond to the theoretical values, i.e. linear fit. It is observed that the linear dependence of Δp with $2/R$ is retrieved.
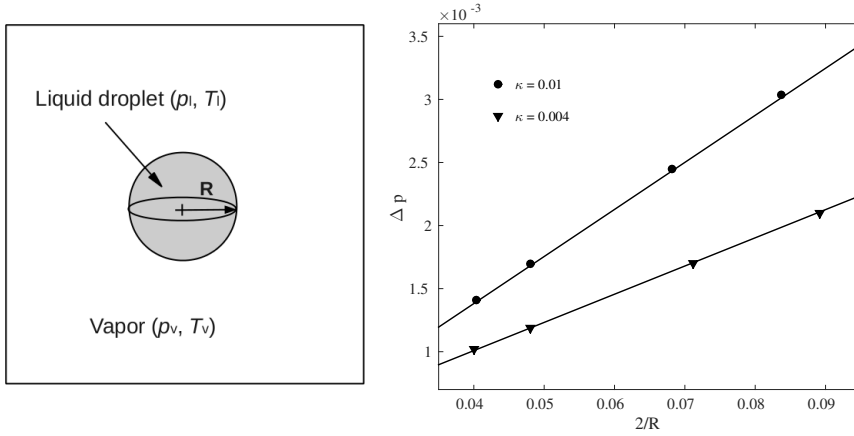
FIGURE 3.1. (left) Schematic of a liquid droplet suspended in vapor phase; (right) Verification of the Young-Laplace law for different surface tensions, taken from Albernaz *et al.* (2016a).

3.2. Marangoni effect

Surface effects play a critical role in many kinetic process of materials and can even drive the flow by tangential gradients of surface tension, known as the Marangoni effect (Marangoni (1871)). Surface tension depends on the temperature T, solute concentration c and surfactant concentration. Neglecting surfactant effects, surface tension variations can be therefore defined as

$$d\sigma(T, c) = \frac{\partial \sigma}{\partial T}dT + \frac{\partial \sigma}{\partial c}dc \ . \tag{3.2}$$

When the solute concentration drives the variation of the surface tension, the Marangoni effect is referred to as the solutocapillary effect. In cases where the surface tension changes with the temperature, the Marangoni effect is denoted as the thermocapillary effect. Both effects can coexist depending on the conditions. Figure 3.2 shows the variation of surface tension as a function of temperature. The numerical results are compared to normalized experimental data of a hexane fluid where a very good agreement can be seen. The general trend is that surface tension decreases with the increase of temperature. The thermal dependence of the surface tension is defined as $\sigma_T = d\sigma/dT$, which is directly obtained from the plot in Fig. 3.2 for a hexane fluid.

An example of how the surface tension gradient can give rise to a bulk fluid motion is shown in Fig. 3.3 and was studied by Levich (1962). An open rectangular container is considered with a very thin liquid layer at the bottom, where one of the sidewalls has a higher constant temperature T_H than the other side, characterized with a constant temperature T_L.
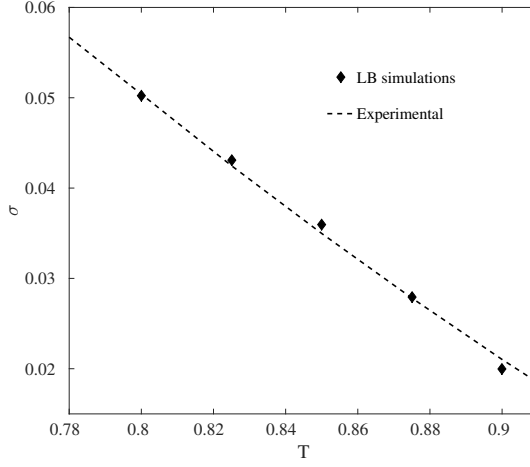
FIGURE 3.2. The surface tension is plotted as a function of the reduced temperature. Comparison between numerical results and experimental data for a hexane fluid taken from Albernaz *et al.* (2016a).
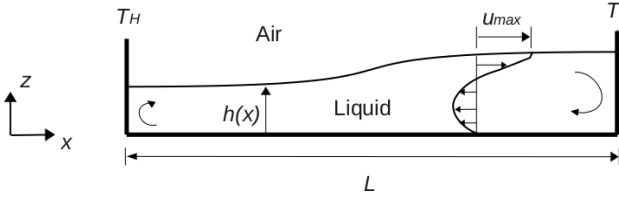

FIGURE 3.3. Thermocapillary motion in a shallow water.

The difference in side wall temperatures results in a temperature gradient along the surface and a corresponding surface temperature gradient in the x direction. The variation of surface tension is maintained and a thermocapillary motion is generated at the interface, where the fluid height h is a function of the distance, i.e. $h(x)$. To illustrate this, we assume a low Re number and neglect inertial terms, as well as lateral velocity gradients. For a steady two-dimensional incompressible flow, with constant liquid viscosity, the momentum equation in the x direction reduces to the Couette form

$$\frac{\partial p}{\partial x} = \mu \frac{\partial^2 u}{\partial z^2} \ , \tag{3.3}$$

and the z momentum equation without surface curvature effects is given as

$$\frac{\partial p}{\partial z} = -\rho g \ . \tag{3.4}$$

The integral form of the continuity equation for the fully developed flow is

$$\int_0^{h(x)} u(z)dz = 0 \ , \tag{3.5}$$

where the liquid surface layer is set in motion by the surface tension force, which generates a displacement of the fluid in the opposite direction below the surface, as sketched in Fig. 3.3. It is important to note that the Marangoni force acts from regions of low to high surface tension. The thermally induced Marangoni force relates the normal component of the shear stress to the tangential derivative of the temperature. At the interface, with curvature neglected, it is written as:

$$\mu \frac{\partial u}{\partial z} = \frac{d\sigma}{dx} \quad \text{at} \ \ z = h(x) \ . \tag{3.6}$$

A no-slip boundary condition is given at the bottom, i.e. $u(z = 0) = 0$. The liquid velocity has a maximum value u_{max} at the interface, which can be obtained after some mathematical manipulations from the equations above as (Probstein (1994))

$$u_{max} = \frac{h}{4\mu} \frac{d\sigma}{dx} \ , \tag{3.7}$$

which is given as a function of the driving force $d\sigma/dx$. Gradients in surface tension can also lead to instabilities, with subsequent cellular-type flows, as widely investigated for Bénard-Marangoni instability (Guyon *et al.* (2001)). It is important to note that one could relate Eq. (3.2) to (3.6), obtaining

$$\mu \frac{\partial u}{\partial z} = \sigma_T \frac{dT}{dx} \ , \tag{3.8}$$

where the shear stresses are explicitly balanced by the physical parameter σ_T times the temperature gradient. This type of relation consists of a boundary condition that acts at the free surface of the fluid (typically a gas-liquid interface) and will be further used to discuss the internal circulation of a droplet caused by thermocapillary effects. The motion obtained at the droplet surface due to differences in surface tension can be a mechanism to generate this internal flow.

CHAPTER 4

Turbulence

Turbulence appears much more often than we realize. Its presence may be desirable, e.g. for applications as the mixing of different reactants in combustion devices, where mixing has to occur as rapidly as possible, or undesirable, e.g. when drag is increased. An essential feature of turbulent flows is that the fluid velocity field varies significantly and irregularly in both position and time. In this type of flow, unsteady vortices appear on many scales and interact with each other, where the transport and mixing are much more effective than in the laminar regime. For a laminar case, the fluid flows in parallel layers.

Richardson (1922) was the first to realize that turbulence is composed by eddies of different sizes. Large eddies are unstable and break down into smaller ones that undergo a similar breakup process, so that energy is transferred toward smaller scales, until kinetic energy is converted into heat at the smallest scales of motion, where viscosity dominates. This is the concept of an *energy cascade*, with energy transfer across several scales until molecular viscosity is effective in dissipating the kinetic energy into internal energy. Kolmogorov (1941a) proposed hypotheses that led to the most important contribution to quantitative statistical description of turbulent flows. In the first hypothesis, he postulated that for high Reynolds numbers, the small-scale turbulent motions are statistically isotropic. In general, large eddies are anisotropic and are affected by the boundary conditions of the flow (Pope 2000). Kolmogorov argued that the smaller eddies lose any preferred orientation, obtaining a local isotropy that is independent of the large-scale motions. The statistics of small scales are universally dependent on the kinematic viscosity ν and the rate of energy dissipation ε. With only these two parameters, a length scale can be obtained by dimensional analysis as

$$\eta = \left(\frac{\nu^3}{\varepsilon}\right)^{1/4} \, , \qquad (4.1)$$

where η is known as the Kolmogorov length scale. The respective Kolmogorov velocity and time scales are $u_\eta = (\varepsilon\nu)^{1/4}$ and $t_\eta = (\nu/\varepsilon)^{1/2}$. These scales characterize the smallest, dissipative eddies. The Reynolds number based on these scales is unity, i.e. $Re_\eta = \eta u_\eta/\nu = 1$, indicating that viscous stresses and inertial forces balance at this level.

A turbulent flow can also be viewed as a superposition of a spectrum of velocity fluctuations and eddies upon a mean flow. A convenient way to deal mathematically with turbulent quantitites is to separate between the average and fluctuating parts. This splitting is known as a Reynolds decomposition, which assumes e.g. for velocity u_i

$$u_i = \overline{u_i} + u'_i \; , \tag{4.2}$$

where $\overline{u_i}$ denotes the time average and u'_i the fluctuation part. In order to obtain the equation of motion for turbulent flows, we assume an incompressible Navier-Stokes equation with a total instantaneous velocity given by

$$\frac{\partial u_i}{\partial t} + u_j \frac{\partial u_i}{\partial x_j} = -\frac{1}{\rho}\frac{\partial p}{\partial x_i} + \nu \frac{\partial^2 u_i}{\partial x_j \partial x_j} \; , \tag{4.3}$$

where density ρ is considered constant. Introducing the Reynolds decomposition for the velocity and pressure quantities, and taking the average gives

$$\frac{\partial \overline{u_i}}{\partial t} + \overline{(\overline{u_j} + u'_j)\frac{\partial (\overline{u_i} + u'_i)}{\partial x_j}} = -\frac{1}{\rho}\frac{\partial \overline{p}}{\partial x_i} + \nu \frac{\partial^2 \overline{u_i}}{\partial x_j \partial x_j} \; . \tag{4.4}$$

The average of the fluctuating part and its derivatives are zero. For the incompressible condition $\partial u_i / \partial x_i = 0$, Eq. (4.4) can be rewritten as

$$\frac{\partial \overline{u_i}}{\partial t} + +\overline{u_j}\frac{\partial \overline{u_i}}{\partial x_j} = -\frac{1}{\rho}\frac{\partial \overline{p}}{\partial x_i} + \frac{\partial}{\partial x_j}\left(\nu \frac{\partial \overline{u_i}}{\partial x_j} - \overline{u'_i u'_j}\right) \; . \tag{4.5}$$

Equation (4.5) is known as the Reynolds-averaged Navier-Stokes (RANS) equation, first proposed by Reynolds (1895). The change in mean momentum due to the unsteadiness and convection of the mean flow is represented in the left hand side of Eq. (4.5). The right hand side gives, respectively, the isotropic stress owing to the mean pressure field, the viscous stresses, and apparent stress owing to the fluctuating velocity field. This last term is referred to as the Reynolds stress. It consists of a nonlinear tensor with symmetric properties, which has led to the creation of many different turbulence models. By isolating the trace of this tensor one obtains the kinetic energy (per unit mass) of the turbulent fluctuations, defined as

$$E = \frac{1}{2}\overline{u'_i u'_i} = \frac{1}{2}\left(\overline{u_1'^2} + \overline{u_2'^2} + \overline{u_3'^2}\right) \; . \tag{4.6}$$

The turbulent kinetic energy can also be expressed in terms of the integral over wavenumber space, giving

$$E = \int_0^\infty E(k)dk \; , \tag{4.7}$$

where k denotes the wavenumber.

4.1. Homogeneous isotropic turbulence

Isotropic turbulence by direct numerical simulation has been extensively studied (Ishihara *et al.* 2009). Homogeneity ensures that there are no gradients in the mean turbulence statistics (invariance in translation) whereas isotropy leads to absence of anisotropy, i.e. no mean shear or buoyancy effects (invariance in rotation). Stationary turbulence is created by inserting energy into the flow field through the low wavenumber modes so that a turbulent cascade develops as statistical equilibrium is reached.

In a DNS of homogeneous isotropic turbulence, the solution domain is a cube of side L with periodic boundary conditions. The lowest non-zero wavenumber in magnitude is $k_0 = 2\pi/L$. The scalar wavenumber is given as $k = (\mathbf{k} \cdot \mathbf{k})^{1/2}$. For a high Reynolds number, the span of lengthscales will also be large and it is possible to find a range of wavelengths that satisfy

$$\eta \ll \frac{2\pi}{k} \ll L , \quad or \quad \frac{1}{L} \ll k \ll \frac{1}{\eta} . \tag{4.8}$$

The viscosity is negligible in this range of wavenumbers, which is known as the inertial subrange. Here, the dominant energy process is the transfer of kinetic energy from large eddies to smaller eddies by inertial forces, known as the inertial subrange. The power spectrum $E(k)$ in this range must be independent of the kinematic viscosity ν and can only depend on ε and k, which assumes

$$E(k) = C\varepsilon^{2/3} k^{-5/3} , \tag{4.9}$$

where C is a universal constant. Equation (4.9) is known as the Kolmogorov $-5/3$ law (Kolmogorov 1941b), and has been widely verified in turbulent flows. Figure 4.1 shows how $E(k)$ is distributed as a function of the wavenumber, where the $-5/3$ slope is seen for the inertial range. Low wavenumbers would correspond to large scales whereas high wavenumbers to smaller ones, i.e., it describes the energy distribution among eddies of different sizes. Energy is transferred successively to smaller scales, where the decay seen in Fig. 4.1 corresponds to the cascade, which takes place over several orders of magnitude. The rate at which the turbulent kinetic energy is dissipated by viscosity is given by

$$\varepsilon = 2\nu \int_0^\infty k^2 E(k) dk . \tag{4.10}$$

The dissipation occurs at high wavenumbers, i.e. at the smallest eddies present so that kinetic energy is dissipated through viscosity. It can also be written as $\varepsilon = \nu \sum_{\mathbf{x}} (\nabla u)^2 / L^3$. The large eddy turnover time scales with $t_L = L/u_{rms}$, u_{rms} being the root mean square of the fluctuating velocity.
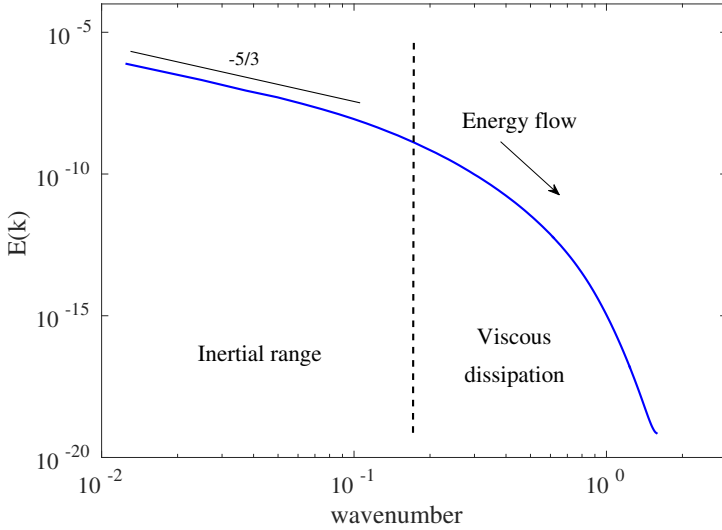
FIGURE 4.1. Energy spectrum as a function of the wavenumber.

Another important length scale is the Taylor microscale, defined in terms of the square root of the ratio between variances of the velocity and velocity gradient, following

$$\lambda = \left[\frac{15 \nu u_{rms}^2}{\varepsilon} \right]^{1/2} . \tag{4.11}$$

The Taylor microscale signifies an intermediate length scale at which fluid viscosity still affects the dynamics of turbulent eddies in the flow, however it is not a dissipative scale. The Taylor microscale is traditionally applied to a turbulent flow, which can be characterized by a Kolmogorov spectrum of velocity fluctuations, as in isotropic turbulence. A Taylor Reynolds number is obtained when considering this microscale, which becomes

$$Re_\lambda = \frac{u_{rms}\lambda}{\nu} . \tag{4.12}$$

Developed isotropic turbulence is illustrated in Figure 4.2 by showing the instantaneous magnitude of the velocity field. The Taylor Reynolds number used in this simulation is $Re_\lambda = 110$.
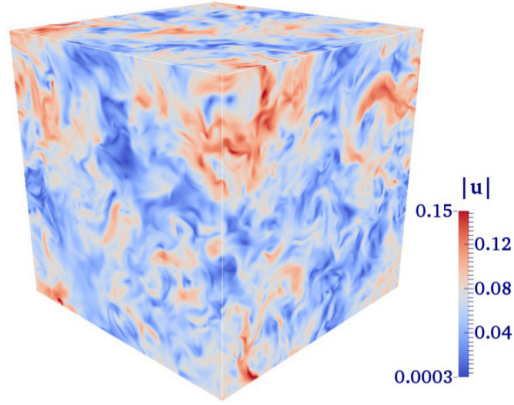
FIGURE 4.2. Magnitude of the instantaneous velocity field in a three-dimensional periodic domain, where $Re_\lambda = 110$.

Numerical method

The numerical simulation of flows with phase change is challenging due to the evolving nature of the fluid-fluid interface. It is essential to couple the interfacial mass transfer, latent heat and surface tension in accordance with the relevant conservation of mass, momentum and energy. There are various numerical schemes which can be used for the direct numerical simulation of gas-liquid flows. For Navier-Stokes solvers, i.e. based on the discretization of macroscopic governing equations, the volume of fluid method (Scardovelli & Zaleski (1999)), level set method (Sethian & Smereka (2003)) and front tracking method (Tryggvason *et al.* (2001)) are the most common methods used.

Different methods have been applied to investigate droplet evaporation. Tanguy *et al.* (2007) developed a level set method associated with the ghost fluid method to enable higher order discretization schemes at the interface. Zhang (2003) and Balaji *et al.* (2011) used a finite volume method where the droplet maintains a spherical shape. A volume of fluid method (VOF) was used by Hase & Weigand (2004) where strong deformations are captured. Schlottke & Weigand (2008) improved the same VOF code to perform direct numerical simulations of droplet evaporation. VOF was also used by Strotos *et al.* (2011) and Banerjee (2013) where a multicomponent droplet was considered. Although each method has a different approach, in order to satisfy conservation conditions, a local vaporizing mass flow rate has to be set explicitly, which is usually done by means of a reference experimental data. An evaporation model often introduces different simplifications, e.g. non deformable droplet (axisymmetric evaporation) or the assumption of constant gas physical properties (quasi-steady). The available evaporation models can be found in reviews by Sazhin (2006) and Erbil (2012).

Unlike the conventional numerical methods previously mentioned, Molecular Dynamics (MD) and lattice Boltzmann method (LBM) are two methods where no tracking method is needed for generating an interface. The phase segregation can emerge naturally as a result of particle interactions. MD is used for simulating the physical movements of atoms and molecules, where many degrees of freedom are present. A common method in this category is the Monte Carlo molecular method, which is based on states according to appropriate Boltzmann probabilities. The drawback of MD is due to the large amount of molecules needed for simulating macroscopic flows and the simulated time, which at present is in the order of nanoseconds.

The LBM is becoming an increasingly important method for simulating multiphase flows (Sukop & Thorne (2006)). It is in the category of diffuse interface methods and is based on a mesoscopic kinetic equation for particle distribution functions (Chen & Doolen (1998)). The mesoscopic approach is a simplification of MD, where instead of simulating every molecule one takes into consideration a group of molecules which are confined at nodes and move in a discrete number of directions, as illustrated in Fig. 5.1. By averaging the kinetic equations one reproduces the Navier-Stokes equations at the macroscopic level.
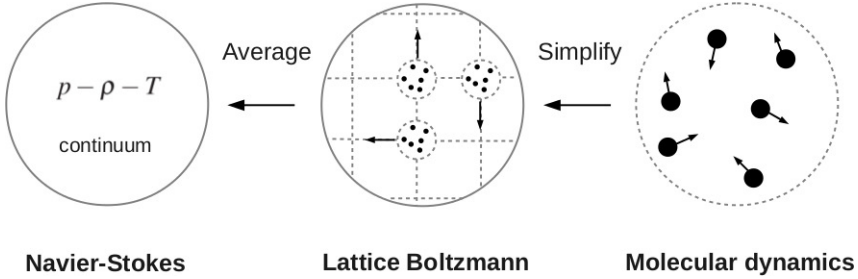

FIGURE 5.1. Macro-, meso- and microscale for the numerical modelling.

The mesoscopic nature of LBM includes only a minimal amount of microscopic details in order to reproduce interfacial physics and macroscopic flow hydrodynamics in a consistent manner (Safari *et al.* (2013)). Its nature is therefore responsible for avoiding the need for tracking the interface as it bridges microscopic phenomena and the macroscopic scale. It also presents a convenient framework to incorporate thermodynamic effects, which naturally generate the phase separation. The kinetic equation provides also the advantages of easy implementation of boundary conditions and fully parallel algorithms. Because of the current availability of fast and massively parallel machines, there is a trend to use codes that can exploit the intrinsic features of parallelism, which is the case of the LBM.

5.1. The lattice Boltzmann method

The lattice Boltzmann model is constructed as a simplified, fictitious molecular dynamics method in which space, time, and particle velocities are all discrete. In other words, the LBM vastly simplifies Boltzmann's original conceptual view by reducing both the number of possible particle spatial positions and the continuum microscopic momenta. Particle positions are confined to the nodes of the lattice, which is characterized as a regular grid. The lattice Boltzmann equation is given by

$$f_i(\mathbf{x} + \mathbf{c}_i\delta_t, t + \delta_t) - f(\mathbf{x}, t) = \delta_t\Omega_i + \delta_t F_i' \ , \tag{5.1}$$

where f_i is the density distribution function, t is time and δ_t is the time step. The lattice velocity is given by $\mathbf{c}_i$, $\mathbf{x}$ is the spatial position and F' is an external

forcing term, which can include e.g. gravity forces or interparticle interactions. The change of f_i due to collisions is represented by Ω_i. The notation i is given as $i = 0, \ldots, N$, where N denotes the number of directions of the particle velocities at each node. For two-dimensional simulations a lattice with nine-velocity directions is recommended (D2Q9), while a nineteen-velocity lattice is usually applied for three-dimensional calculations (D3Q19).

Starting from an initial state, the configuration of particles at each time step evolves in two sequential sub-steps, described as *(i) streaming*, which is given by the LHS of Eq. (5.1), where each particle moves to the nearest node in the direction of its velocity; and *(ii) collision*, which occurs when particles arriving at a node interact and change their velocity directions according to scattering rules. It is important to note that the streaming process of the LBM is linear. This feature comes directly from the kinetic theory and contrasts with the nonlinear convection terms in other numerical approaches that use a macroscopic representation. Simple convection combined with a collision operator allows the recovery of the nonlinear macroscopic advection through multi-scale expansions, which turns out to be one big advantage when dealing with LBM. The macroscopic fluid quantities, such as density and velocity, are calculated by

$$\rho = \sum_{i=0}^{N} f_i \ , \quad \mathbf{u} = \frac{1}{\rho} \sum_{i=0}^{N} \mathbf{c}_i f_i \ . \tag{5.2}$$

The macroscopic velocity $\mathbf{u}$ is an average of the discretized microscopic velocities $\mathbf{c}_i$ weighted by the directional densities f_i. Different collision operators have been proposed. A simple linearized version of the collision operator makes use of a relaxation time towards the local equilibrium using a single time relaxation. This collision model is known as the Bhatnagar-Gross-Krook (BGK), which was proposed by Bhatnagar *et al.* (1954) and is written as

$$\Omega_i = -\frac{f_i - f_i^{eq}}{\tau_f} \ , \tag{5.3}$$

where f^{eq} is a local equilibrium distribution, which has to be formulated so that the Navier-Stokes equations are recovered in the macroscopic scale. In order to do so, the equilibrium function has to be defined as

$$f_i^{eq} = \omega_i \rho \left[1 + \frac{\mathbf{c}_i \cdot \mathbf{u}}{c_s^2} + \frac{(\mathbf{c}_i \cdot \mathbf{u})^2}{2c_s^4} - \frac{\mathbf{u} \cdot \mathbf{u}}{2c_s^2} \right] \ , \tag{5.4}$$

where c_s is the sound speed and ω_i are the weights according to the lattice chosen. By using the BGK collision operator, the kinematic viscosity ν is denoted as

$$\nu = c_s^2 (\tau_f - 1/2) \ . \tag{5.5}$$

We would like to mention that although the BGK model is widely used due to its simplicity, it is numerically unstable under certain conditions, e.g. for high Reynolds numbers where lower values of the fluid viscosity are necessary. This can be solved by using a more robust collision operator. The multiple-relaxation-time model (MRT) proposed by Lallemand & Luo (2000) allows for different physical quantities to be adjusted independently and has shown significant improvement in the numerical stability. If body forces acting on a fluid are absent, i.e. $F_i' = 0$ in Eq. (5.1), the equation of state for this model assumes the form as for an ideal gas, where

$$p = \rho c_s^2 \; . \tag{5.6}$$

However, with the idea of simulating a vapor-liquid flow, F_i' should be used. In LBM, the phase segregation can be modelled by an interaction force, i.e. a special mesoscospic force which acts between every pair of neighboring nodes. Shan & Chen (1993) proposed the pseudopotential model, where this interaction force is calculated from an interaction potential ψ. For single-component multiphase flows, the force is given by

$$\mathbf{F} = \psi(\rho(\mathbf{x}))G \sum_{i=1}^{N} \psi(\rho(\mathbf{x} + \mathbf{c}_i))\mathbf{c}_i \; , \tag{5.7}$$

where G is the interaction strength. We note that the potential is dependent on the local fluid density. For this force, the equation of state (EOS) has the form (He & Doolen (2002))

$$p = \rho c_s^2 - \frac{Gc^2}{2}\Psi^2 \; , \tag{5.8}$$

where c is a lattice constant. Many discussions have been made on how to choose the potential ψ. The only way to satisfy both the mechanical stability solution (Maxwell construction) and the thermodynamic theory is if $\psi \propto \exp(-1/\rho)$, as shown by Shan & Chen (1994). If one wants to include an arbitrary EOS, a different approach is recommended. We adopted a method proposed by Kupershtokh *et al.* (2009), where the force is given as

$$\mathbf{F} = 2\Phi\nabla\Phi, \tag{5.9}$$

where Φ is a special function written as

$$\Phi = \sqrt{\rho c_s^2 - \kappa p(\rho, T)} \; , \tag{5.10}$$

here $p(\rho, T)$ can be based on an arbitrary EOS. The term κ denotes a dimensionless parameter that controls the interface thickness in lattice units. Kupershtokh *et al.* (2009) also proposed a numerical approximation for the local

force based on a linear combination of the local and the mean value gradient approximations, calculated by

$$\mathbf{F} = \frac{A}{c_s^2} \sum_{i=1}^{N} \lambda_i \Phi^2(\mathbf{x} + \mathbf{c}_i)\mathbf{c}_i + \frac{(1 - 2A)}{c_s^2} \Phi(\mathbf{x}) \sum_{i=1}^{N} \lambda_i \Phi(\mathbf{x} + \mathbf{c}_i)\mathbf{c}_i \, , \qquad (5.11)$$

where A is a correlative fitting parameter that allows a better fit with the coexistence curve for the desired fluid, satisfying the Maxwell construction. The value of A changes according to the EOS adopted. Equation (5.11) is a numerical approximation for the local force based on a linear combination of the local and the mean value gradient and improves the numerical stability, where the spurious currents around the interface are significantly reduced. These currents are a common problem in simulations with free boundaries. The use of Eq. (5.11) is followed by the definition of F_i' in Eq. (5.1) as

$$F_i' = f_i^{eq}(\rho, \mathbf{u} + \Delta\mathbf{u}) - f_i^{eq}(\rho, \mathbf{u}) \, , \qquad (5.12)$$

where $\Delta\mathbf{u} = \mathbf{F}/\rho$. Equation (5.12) describes the exact difference method (EDM) and was proposed by Kupershtokh & Medvedev (2006). It can also be rewritten as (Shan *et al.* (2006))

$$F_i' = \omega_i \left[\frac{\mathbf{c}_i \cdot \mathbf{F}}{c_s^2} + \frac{(\mathbf{c}_i \cdot \mathbf{v})(\mathbf{c}_i \cdot \mathbf{F})}{c_s^4} - \frac{\mathbf{v} \cdot \mathbf{F}}{c_s^2} \right] \, . \qquad (5.13)$$

Due to the presence of the body force F_i', the actual fluid velocity $\mathbf{v}$ should be taken at half time step, i.e. averaging the momentum before and after collision, giving

$$\mathbf{v} = \mathbf{u} + \frac{\mathbf{F}}{2\rho} \, . \qquad (5.14)$$

Although it is possible to show that the total momentum in the whole computational domain is conserved, the momentum is not conserved locally when an interparticle force model is used. As a result, spurious velocities appear in regions adjacent to the interface. The velocity field for an equilibrium condition between a liquid droplet and vapor is shown in Fig. 5.2. The radius is represented by the solid circle. The unphysical spurious currents can be observed, where the maximum value is around the interface. The increase of these currents may cause numerical instabilities and departure from real fluid conditions, more prominent when a BGK model is used. The maximum spurious velocity observed in this equilibrium condition is $|v_{max}| \sim 10^{-4}$. Our simulations showed that not only higher density ratio contribute to the increase of spurious currents (as reported in Yuan & Schaefer (2006)) but also sharper interfaces.
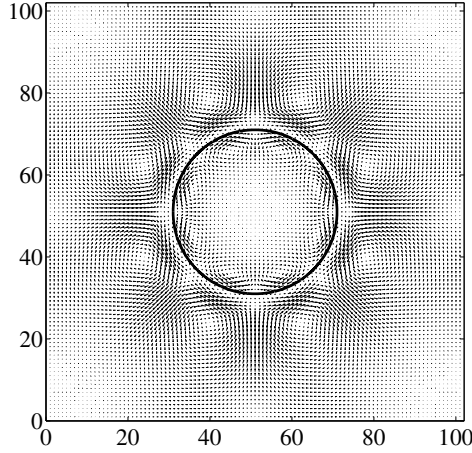
FIGURE 5.2. Velocity field for an equilibrium condition, where $T_r = 0.85$. The maximum velocity is $|v_{max}| \sim 10^{-4}$. Taken from Albernaz *et al.* (2013).

Through a Chapman-Enskog (C-E) analysis, the mass and momentum conservation equations are obtained at the macroscopic scale, given respectively as (Chin (2001))

$$\frac{\partial \rho}{\partial t} + \nabla \cdot (\rho \mathbf{v}) = 0 \ , \qquad (5.15)$$

$$\frac{\partial}{\partial t}(\rho \mathbf{v}) + \nabla \cdot (\rho \mathbf{v} \mathbf{v}) = -\nabla p + \nabla \cdot (2\mu \mathbf{S}) + \mathbf{F}' \ , \qquad (5.16)$$

where μ is the dynamic viscosity and $\mathbf{S} = (\nabla \mathbf{v} + (\nabla \mathbf{v})^T)/2$ the deviatoric stress. The pressure of the LBM is therefore calculated using an equation of state. In contrast, in the direct numerical simulation of incompressible Navier-Stokes equations, the pressure satisfies a Poisson equation with velocity gradients acting as sources. Solving this equation for the pressure often produces numerical difficulties that require special treatment. This has shown to be another advantage of using LBM instead of conventional macroscopic methods.

5.2. Energy equation

The energy equation can be given in terms of the fluid temperature T. For a Newtonian fluid, this equation is given as (Bird (1960))

$$\rho c_v \frac{DT}{Dt} = \nabla \cdot (k\nabla T) - T \left(\frac{\partial p}{\partial T} \right)_\rho \nabla \cdot \mathbf{u} + \mu \Phi_v \ , \qquad (5.17)$$

here c_v is the specific heat at constant volume and k is the thermal conductivity.

The quantity Φ_v is known as the dissipation function and assumes, for a three-dimensional case,

$$
\begin{aligned}
\Phi_v \;=\; & 2\left[\left(\frac{\partial u_x}{\partial x}\right)^2 + \left(\frac{\partial u_y}{\partial y}\right)^2 + \left(\frac{\partial u_z}{\partial z}\right)^2\right] + \left(\frac{\partial u_y}{\partial x} + \frac{\partial u_x}{\partial y}\right)^2 \\
& + \left(\frac{\partial u_z}{\partial y} + \frac{\partial u_y}{\partial z}\right)^2 + \left(\frac{\partial u_x}{\partial z} + \frac{\partial u_z}{\partial x}\right)^2 - \frac{2}{3}\left(\frac{\partial u_x}{\partial x} + \frac{\partial u_y}{\partial y} + \frac{\partial u_z}{\partial z}\right)^2
\end{aligned}
\tag{5.18}
$$

Multiphase LBM have been used widely in isothermal flow simulations (e.g. Sbragaglia *et al.* (2009); Wagner & Yeomas (1999)). Recently, thermodynamic effects with phase change have been considered in the LBM perspective by different schemes (Gan *et al.* (2012)). Among the thermal LB models for multiphase flows proposed, the multispeed (Gonnella *et al.* (2007)) and passive scalar (Zhang & Chen (2003)) approaches stand out. The multispeed approach assures energy conservation at a mesoscopic level, introducing the energy as a moment of distribution functions and enlarging the number of discrete speeds of the distribution functions in order to achieve the proper symmetries for the internal energy flux. This approach comes with a higher computational cost. Throughout this work we use the passive scalar approach, where the temperature field is advected passively by the fluid flow, so the coupling between energy and momentum is done at the macroscopic level. Moreover, this approach is numerically more stable than the multispeed one.

By solving the temperature as a passive scalar, one can use the hybrid scheme, where Eq. (5.17) is solved by finite difference scheme. In order to do so, Eq. (5.17) is rewritten with a forward Euler scheme as (Albernaz *et al.* (2016b))

$$
\begin{aligned}
T(\mathbf{x}, t+1) \;=\; & T(\mathbf{x}, t) - \mathbf{v}\cdot\nabla^+ T + \frac{1}{\rho c_v}\nabla^+ k\nabla^+ T + \alpha\Delta^+ T \\
& - \frac{T}{\rho c_v}\left(\frac{\partial p}{\partial T}\right)_\rho \nabla^+\cdot\mathbf{v} + \frac{\nu}{c_v}\Phi_v \;,
\end{aligned}
\tag{5.19}
$$

where $\alpha = k/(\rho c_v)$ denotes the thermal diffusivity and the superscript $+$ corresponds to the finite difference operators. Equation (5.19) was used for solving problems where turbulence is considered (Papers 4 and 5). One could also solve Eq. (5.17) by employing a double distribution function (DDF) scheme (Márkus & Házi (2011)) where a second distribution function is used for monitoring the temperature field. This distribution can be given as

$$
g_i(\mathbf{x} + \mathbf{c}_i\delta_t, t + \delta_t) = g_i(\mathbf{x}, t) - \frac{1}{\tau_g}(g_i - g_i^{eq}) + C_i \;,
\tag{5.20}
$$

where C_i is a correction term and g_i^{eq} denotes the equilibrium distribution function. The temperature is evaluated by

$$T = \sum_i g_i .$$
(5.21)

The equilibrium function is written as

$$g_i^{eq} = \omega_i T (1 + 3\mathbf{c}_i \cdot \mathbf{v}) .$$
(5.22)

In order to obtain Eq. (5.17), the correction term C_i needs to assume

$$C_i = \omega_i \left[\frac{\nabla \cdot (k \nabla T)}{\rho c_v} - \alpha^{LB} \nabla^2 T + \frac{\nu}{c_v} \Phi_v \right] + \omega_i T \left[1 - \frac{1}{\rho c_v} \left(\frac{\partial p}{\partial T} \right)_\rho \right] \nabla \cdot \mathbf{v} ,$$
(5.23)

where $\alpha^{LB} = (\tau_g - 1/2)/3$ is the lattice thermal diffusivity.

5.3. Validations and tests

In order to check the behavior of the physical properties as functions of the different parameters, we simulated first a static suspended droplet in thermodynamic equilibrium with its surrounding vapor, i.e. where no mass transfer occurs. Thermodynamic variables are shown with reduced values and remaining quantities are given in lattice units (l.u.), where reference length corresponds to the lattice spacing δ_x and time to δ_t. The boundaries are periodic, with 2D simulations performed for a domain of 300×300 (l.u.). The influence of the parameters T_r, τ_f and κ are listed in Table 5.1. Surface tension σ is obtained by Young-Laplace law (as seen on Chapter 3). The increase of κ produces a thinner interface thickness l_i where surface tension is weaker. The maximum velocity v_{max}, which represents the spurious currents in the equilibrium condition, is enhanced either by a thinner interface or by reducing the relaxation time τ_f.

case	T_r	τ_f	κ	σ (l.u.)	l_i (l.u.)	v_{max} (l.u.)	ρ_ℓ/ρ_v
1	0.80	0.5813	0.010	0.1030	5	$4.9e-4$	36.5
2	0.85	0.5813	0.005	0.1208	11	$1.1e-4$	19.4
3	0.85	0.5813	0.010	0.0852	6	$3.8e-4$	19.6
4	0.85	0.5208	0.010	0.0850	6	$2.1e-3$	19.6
5	0.90	0.5813	0.010	0.0468	8	$1.3e-4$	9.9

TABLE 5.1. Physical properties according to the reduced temperature T_r, relaxation time τ_f and κ.

We observe that the density ratio ρ_ℓ/ρ_v is independent of τ_f, for the same T_r and κ. Furthermore, for lower values of τ_f the computational time needed to achieve equilibrium is raised. When T_r increases, for the same κ, the interface is thicker, which is expected as it gets closer to the critical point. It is important to mention that these results were performed using a MRT collision operator. If a BGK model is employed to simulate the same static droplet with the relaxation times used in Table 5.1, the computations become unstable. The dynamics of phase change had also to be validated, which is done by means of a static radial droplet evaporation only due to diffusion. The analytical solution for the droplet evaporation rate obtained in section 2.3 is compared to the numerical results.

In order to simulate a static droplet evaporation, the droplet is first equilibrated with the vapor at the saturated temperature in a periodic domain. Then, outflow boundaries are used, where Neumann boundary condition is applied to the velocity. The temperature is then gently raised at the boundaries, set by a Dirichlet boundary condition. To keep the pressure $p(\rho, T)$ constant, density is also set as DBC, calculated by the P-R EOS for a given initial pressure and current temperature. The heat-up of the surrounding vapor, i.e. the conduction of heat through the boundaries to the vapor phase toward the droplet interface takes $t \sim 5 \times 10^4$. After this heat-up phase, the droplet evaporation is analyzed. We observe that a symmetric radial flow is obtained, where no artificial heating occurs. Consistent droplet evaporation was seen even for relatively high density ratio, $\rho_\ell/\rho_v \cong 130$, for $T_r = 0.7$.

Figure 5.3 compares the solution of the D^2 law, Eq. (2.18), here adapted for the 2D coordinates, to the numerical results using $D_0 = 60$ l.u., $D_\infty = 300$, $\alpha_i = 0.0223$ and Spalding number $B = 0.431$. We make use of the parameters defined for cases 2 and 3 in Table 5.1, where only the thickness of the interface is changed. The spurious currents for case 2 are almost four times smaller than for case 3. Nevertheless, we observe that our model is able to produce the correct evaporation rate for both interface thicknesses. Since the static droplet evaporation occurs only due to diffusion, the results indicate that the spurious currents do not influence the evaporation rate. As the droplet shrinks, case 2 shows slight deviation from the D^2 law. This is expected since the interface thickness is of the order of the droplet size, where an overestimation of diffusion occurs. Therefore, it is important to be aware of the accuracy of the results based on the relation between the droplet size and interface thickness.

It is also important to show that the mass transfer rate in the simulations are consistent with the latent heat, given by the jump condition in Eq. (2.13) and included in the analytical solution through the Spalding number B. The latent heat L_{hv} is obtained from hexane properties (Lemmon *et al.* (2013)), being $L_{hv}(T = 0.8) = 0.51$, $L_{hv}(T = 0.85) = 0.45$ and $L_{hv}(T = 0.9) = 0.38$. First, it was verified that the same L_{hv} is obtained from the Clausius-Clapeyron relation in Eq. (2.9), with the current Peng-Robinson EOS.
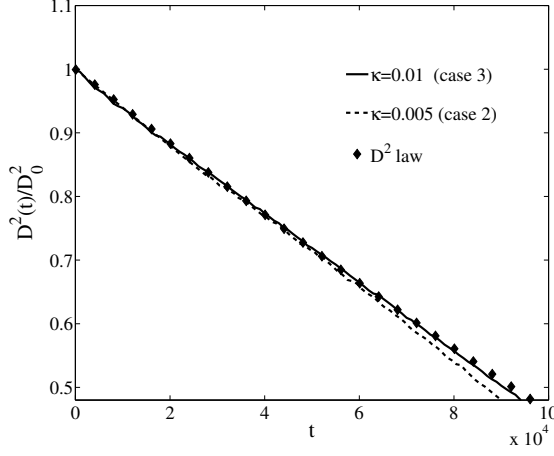
FIGURE 5.3. Normalized square diameter evolution in time, where the D^2 law solution (Eq. (2.18)) and simulation results are shown, for two different interface thicknesses. Taken from Albernaz *et al.* (2015).

We then compare the square diameter evolution between the numerical results and the D^2 law for different latent heat, shown in Fig. 5.4. Here, the temperature difference is kept the same for all cases, $T_\infty - T_i = 0.1$. The numerical results correspond to cases 1, 3 and 5 and are in accordance with the analytical solutions.
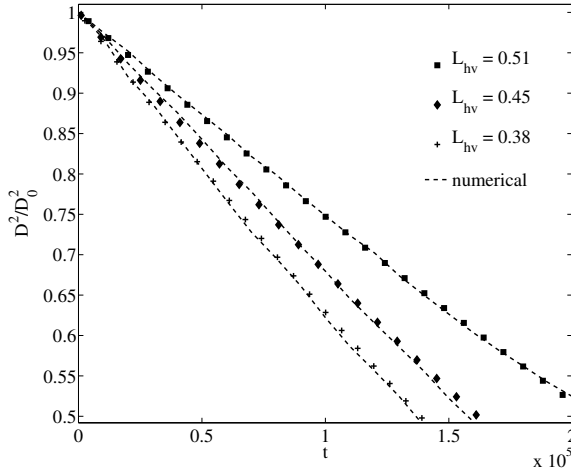

FIGURE 5.4. Comparison between the numerical results and D^2 law of the normalized squared diameter, for different latent heat. Taken from Albernaz *et al.* (2015).

It is seen that an increase of L_{hv} is responsible for a slower evaporation. Such behavior is expected, as more energy is needed to generate the phase change. Figure 5.5 shows the relative error ε between the D^2 law and numerical results as a function of the normalized square diameter. The error is evaluated at the same time-step. Different droplet sizes are tested, where the parameters used correspond to case 3 in Table 5.1. We note that good agreement with the D^2 law is obtained, where the smaller droplet $D_0 = 50$ gives $\varepsilon \cong 1\%$ when $D^2/D_0^2 = 0.5$.
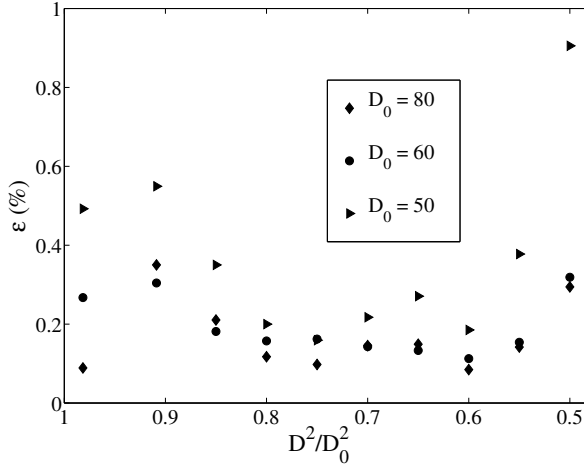

FIGURE 5.5. Error between D^2 law and simulation results, for different droplet sizes. Taken from Albernaz et $al.$ (2015).

CHAPTER 6

Summary of results

We cover in this chapter the main results presented in Part II. Throughout this work we make use of a LBM method that incorporates phase change through a non-ideal equation of state, where a hexane fluid (C_6H_{14}) is considered.

6.1. Forced convection

Results from two-dimensional numerical simulations are reported in Albernaz *et al.* (2013) and Albernaz *et al.* (2015), included as Paper 1 and Paper 2, respectively. Paper 1 deals mostly with model validation, where different equations of state are considered. We observe that the Peng-Robinson EOS suits well for describing a hexane fluid (as seen in Fig. 2.2). Static evaporation is analyzed, without imposing standard evaporation models (Sazhin (2006)), along with gravitational effects. In Paper 2 we have mainly focused on the analysis of a convective flow around a droplet in a Lagrangian frame. We first have validated the latent heat and evaporation rate in our model by comparing it to the D^2 law. The Reynolds number is based on the inlet velocity U and droplet diameter D, assuming $Re = UD/\nu$. We observe the droplet swelling caused by the pressure wave due to the flow initialization. The saturated pressure in the whole domain is shifted by changing the inlet temperature until an equilibrium condition is achieved, where no evaporation or condensation occurs. The evaporation rate is then examined only by means of temperature difference between the incoming vapor and droplet, denoted as ΔT. Raising the superheated vapor temperature decreases the droplet lifetime, as expected.

The increase in Reynolds number can generate an oscillatory behavior in the droplet. We analyze the droplet deformation based on a relation between the droplet width and breadth. Due to the wake-droplet interactions, vortices at the droplet bottom are periodically created and blown away, as shown in Fig. 6.1. The solid circle denotes the droplet interface. First, (a) two symmetric eddies are formed at the droplet bottom region due to the flow separation, where the droplet deformation is maximum. The blowing along the droplet surface induces the detachment of these vortices (b), which are convected along with the vapor flow. The vortices develop and grow in size (c), and droplet deformation reaches a minimum. A backflow is generated by these vortices (d), which assist the formation of new eddies close to the droplet bottom region, completing an oscillatory cycle. Internal circulation is observed inside the droplet. The evaporation rate is seen to increase also when convection is

35

stronger, as the internal circulation enhances heat transfer. Figure 6.2 shows the isotherms along with velocity vectors normal to the droplet surface at the onset of an evaporation case with $\Delta T = 0.002$, where (left) condensation and (right) evaporation take place. A velocity vector pointing outwards means the occurrence of local evaporation whereas if pointing inwards gives an indication of local condensation. While Fig. 6.2 (left) shows condensation at the top and bottom regions, in (right) condensation happens only at the top, with stronger evaporation at the droplet sides. We show that a wider boundary layer (BL) is obtained due to this blowing as shear stresses around the droplet are decreased. We have also computed the velocity in tangential direction along the droplet surface, which supports the effect of local blowing coupled to the BL thickness.
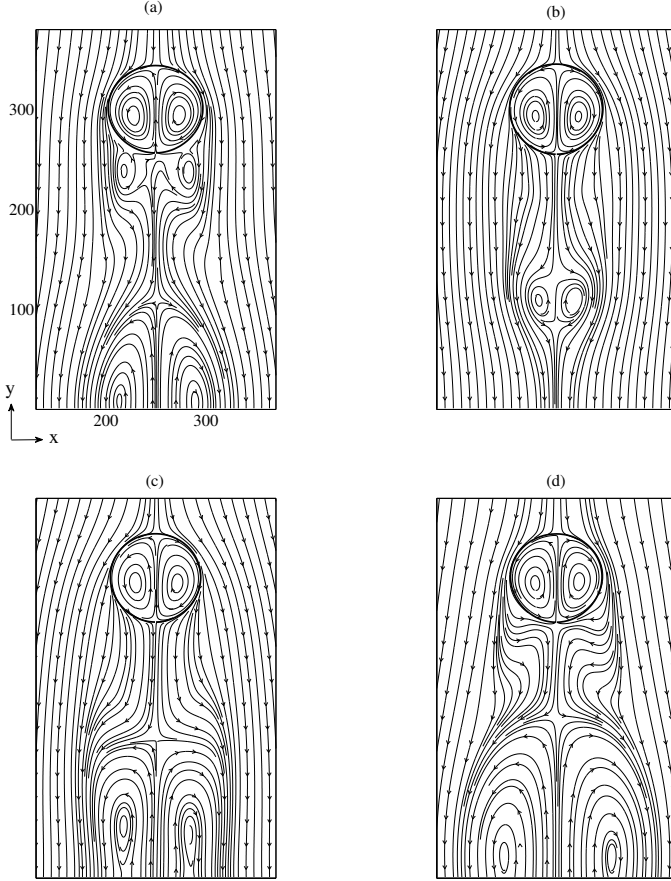

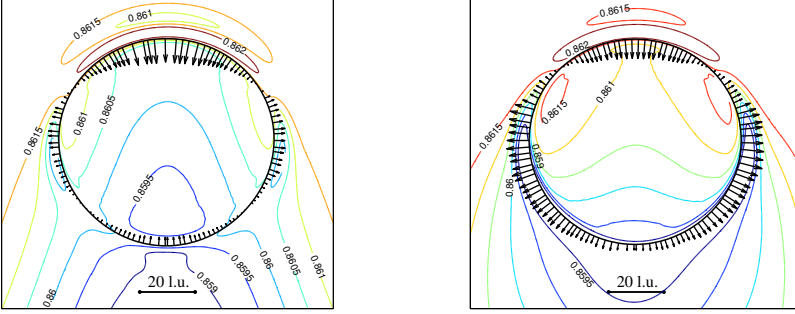FIGURE 6.1. Streamlines for $Re = 130$ and $\Delta T = 0$, taken from Albernaz *et al.* (2015).

FIGURE 6.2. Isotherms and velocity vectors normal to the droplet surface, for $Re = 130$ and $\Delta T = 0.002$, where (left) condensation and (right) evaporation occur. Taken from Albernaz *et al.* (2015).

Three-dimensional simulations of a droplet in forced convection are published in Albernaz *et al.* (2016a), in Part II as Paper 3. We first validate the surface tension under static condition, followed by an investigation of the droplet behavior in a temperature gradient imposed at the motionless surrounding vapor. Marangoni effects drive the droplet displacement due to the surface tension gradient along the interface, caused by the temperature gradient. The droplet center of mass velocity is seen to be proportional to the temperature variation at its surface. We then show results of an evaporative droplet in forced convection, as illustrated in Fig. 6.3, where streamlines indicate a flow in the negative y-direction. Vortices are developed at the droplet rear and vectors represent the flow at the droplet surface.
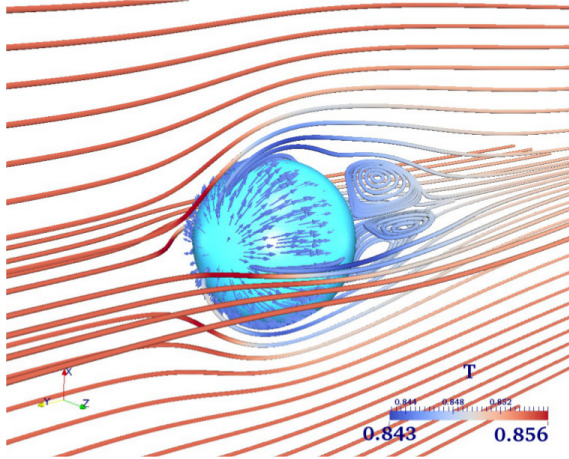

FIGURE 6.3. Forced convection around the droplet taken from Albernaz *et al.* (2016a).
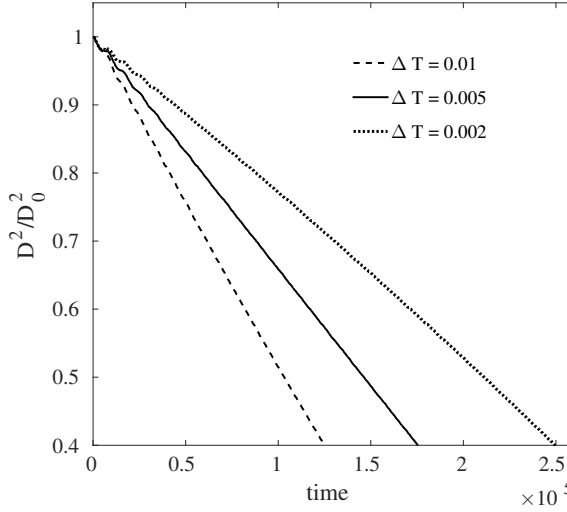
FIGURE 6.4. Squared diameter of the droplet as a function of time, taken from Albernaz *et al.* (2016a).

Figure 6.4 shows the temporal development of the normalized square diameter for different ΔT. The contribution of shear stresses and the Marangoni effect are quantified in Table 6.1, corresponding to the cases in Fig. 6.4 when $D^2/D_0^2 = 0.45$. One can note that the estimation of each effect is similar to the balance in Eq. (3.8), where ΔT_s here assumes the temperature variation at the surface line of half of the droplet $L = \pi D/2$. The Marangoni effect increases with temperature difference, being equivalent to the shear contributions when $\Delta T = 0.01$. It is also important to mention the slight decrease in viscous stresses by raising ΔT. Such behavior is directly related to a stronger evaporation, where the blowing along the droplet surface increases, diminishing the amount of shear stresses. These results reinforce the important relation between the generation of internal circulation by surface tension variations along the droplet and enhancement of the heat transfer, and thus phase change.

ΔT	*Viscous:* $\mu_v \frac{\partial u}{\partial x} \times 10^{-6}$	*Marangoni:* $\sigma_T \frac{\Delta T_s}{L} \times 10^{-6}$
0.002	11.51	4.70
0.005	8.34	6.13
0.010	7.05	7.03

TABLE 6.1. Shear stress and Marangoni effect as a function of ΔT for $D^2/D_0^2 = 0.45$, taken from Albernaz *et al.* (2016a).

6.2. Turbulence with a single phase fluid

Extensive works for turbulent flows with an ideal EOS can be found for both incompressible (Pumir 1994) and compressible cases (Kida & Orzag 1990). Our curiosity was raised when trying to answer the following question: what happens for a real fluid in a turbulent flow when it assumes a temperature and pressure closer to the critical point? In order to answer this, we have analyzed in Albernaz *et al.* (2016b) (Paper 4) a single phase fluid in three-dimensional isotropic turbulence. The fluid is described by a non-ideal EOS allowing us to scrutinize the difference of thermodynamic variables as conditions approach criticality. Figure 6.5 shows the time evolution of temperature fluctuations for the ideal EOS and different temperatures using the PR EOS. The fluctuations are seen to increase with temperature. We have calculated and averaged a normalized pressure fluctuation based on the Reynolds decomposition, and observed fluctuations when $T = 0.98$ to be two orders of magnitude higher than the ones found for the ideal case.
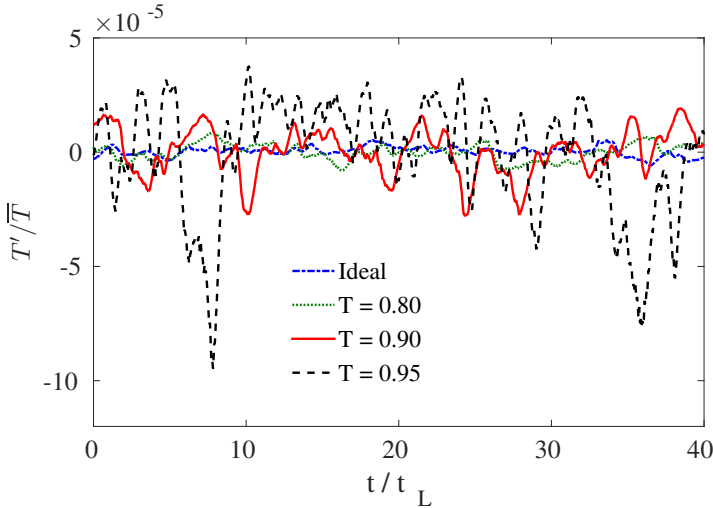

FIGURE 6.5. Turnover time evolution of the temperature fluctuations for $Re_\lambda \approx 110$, taken from Albernaz *et al.* (2016b).

The pressure PDF is shown in Fig. 6.6 for different temperatures. The ideal EOS result is also plotted and compared to data by Donzis & Jagannathan (2013), where good agreement is obtained. We have averaged the whole computational domain over multiple datasets, so that statistically robust information is ensured. For a PR EOS, the behavior for $T = 0.8$ resembles the ideal case. The enhancement of the temperature causes a decrease in the negative pressure fluctuations. While the negative tail narrows, the positive fluctuation seems to be insensitive to the temperature and follows a Gaussian distribution (plotted as dotted lines). The PDFs for density and temperature are seen

to follow the same behavior. We have also analyzed the spectra of thermodynamic variables, where a Kolmogorov $-5/3$ scaling is obtained. A $-7/3$ scaling is observed for the pressure spectra in a narrow region of the inertial range, as reported both experimentally (Tsuji & Ishihara 2003) and numerically (Gotoh & Fukayama 2001). The kinetic energy spectra also shows a $-5/3$ scaling, where the spectrum is independent of the EOS or temperature considered.
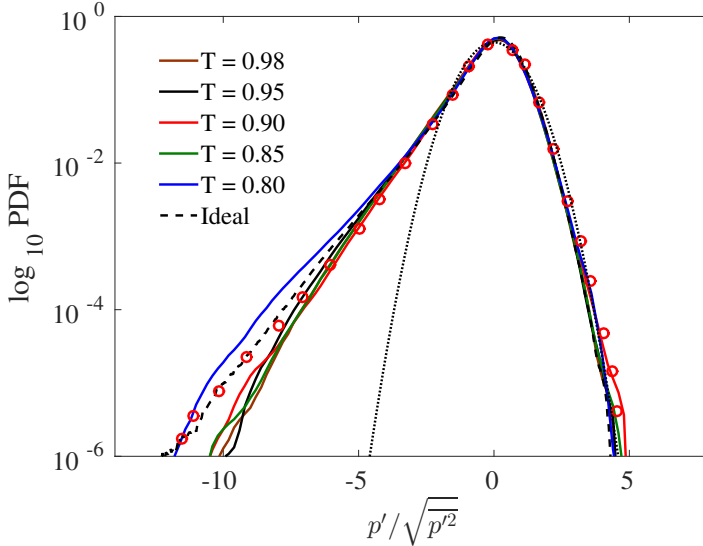

FIGURE 6.6. Semi-log pressure PDF for different temperatures. The dotted curve represents a Gaussian distribution, while data for an Ideal EOS from Donzis & Jagannathan (2013) (circles) is also plotted for comparison. Taken from Albernaz *et al.* (2016b).

We have also examined the effect of the Taylor Reynolds number on the thermodynamic fluctuations, as shown in Fig. 6.7. While the pressure fluctuations for the ideal case are insensitive to Re_λ, the PR EOS shows a different scenario, where fluctuations increase significantly with Re_λ for a condition close to the critical point. This unreported phenomena is more pronounced when analyzing the skewness and flatness factors as a function of Re_λ. For all thermodynamic variables, the skewness (Fig. 6.8 (a)) is seen to increase with Re_λ, whereas flatness (Fig. 6.8 (b)) decreases with Re_λ. This is a clear indication that the PDF of the thermodynamic fluctuations assume a behavior closer to a Gaussian distribution, where a narrower range of fluctuation is obtained. Therefore, we have found that the long negative tails seen for an ideal fluid are not present with a non-ideal EOS when high temperature and Re_λ are considered.
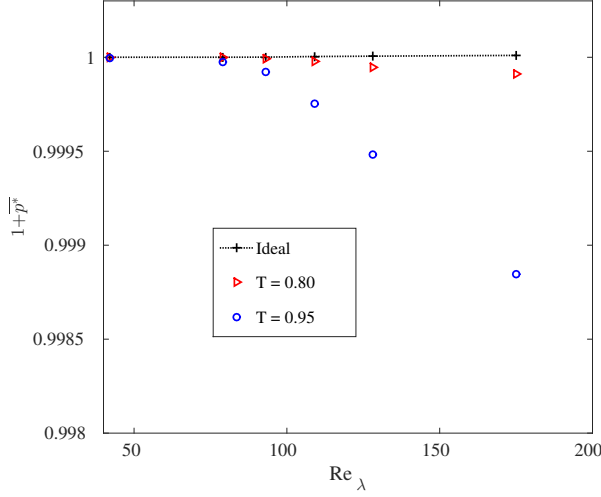
FIGURE 6.7. Pressure fluctuation for different Re_λ, shown for the ideal EOS and PR EOS. Taken from Albernaz *et al.* (2016b).
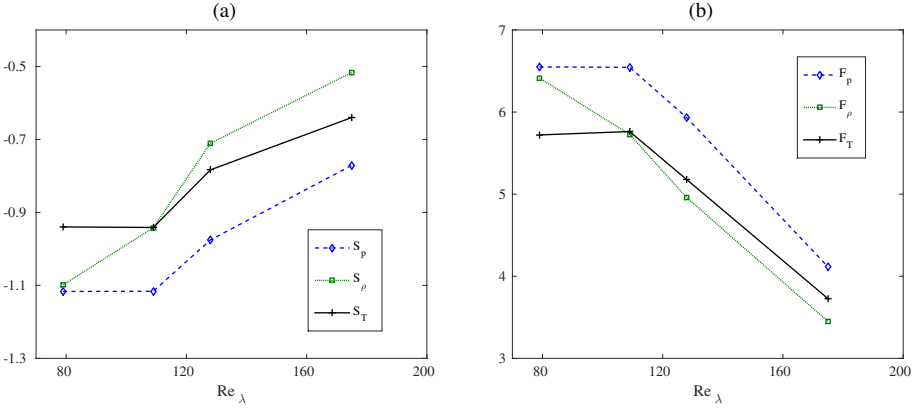

FIGURE 6.8. (a) Skewness and (b) flatness factors for pressure, density and temperature as a function of Re_λ, with $T = 0.95$. Taken from Albernaz *et al.* (2016b).

6.3. Droplet in isotropic turbulence

We have also investigated in Albernaz *et al.* (2016c) (Paper 5) the droplet dynamics in a turbulent environment. The heat and mass transfer between phases are taken into consideration. This study is relevant to fuel sprays in energy conversion systems as well as in nature, e.g. in the rain formation. The primary focus has been to analyze the coupling between turbulence parameters,

thermodynamic variables and droplet dynamics. The density ratio is $\rho_\ell/\rho_v \approx 10$, where the vapor moves faster than the liquid due to the fact that it is lighter. The droplet is displaced and deformed by pressure and shear stress at the interface.

Fluctuations of thermodynamic and turbulence variables are averaged separately for the liquid and vapor phases. Droplet statistics are described in terms of the droplet volume V_d, local Weber number We_d and deformation parameter $S^* = S/S_0 - 1$, where S is the droplet surface area and S_0 the equivalent area of a sphere with the same volume. We also define an Ohnesorge number $Oh = \mu_\ell/(\rho_\ell 2R\sigma)^{1/2}$, where only the surface tension or the droplet radius are changed. We have first performed simulations for a constant Taylor Reynolds number Re_λ. As expected, the amount of deformation grows with lower surface tensions or larger droplet size: the Weber number explains this increase and is seen to be correlated to S^* as found by different authors (Perlekar *et al.* 2012; Qian *et al.* 2006). The droplet volume shows fluctuations that correspond to the presence of evaporation/condensation. The amount of phase change is directly related to the surface tension, droplet size and thermodynamic fluctuations: lower surface tension and larger drop produce a growth in thermodynamic fluctuations and increase the phase change.

We then examine the effects of changing Re_λ and Oh as seen in Table 6.2. The same droplet size is used, which means that different Oh are obtained by changing only the surface tension. Turbulence quantities such as the Taylor length scale λ and Kolmogorov length η decrease by increasing Re_λ, whereas a larger averaged velocity u_{rms} as well as higher dissipation in the liquid phase ε_ℓ are obtained. One should also observe that the turbulence quantities are insensitive to changes in Ohnesorge number (surface tension).

Re_λ	λ	η	$\overline{u_{rms}}$	Oh	$\overline{S^*}$	$\overline{We_d}$	$\overline{\varepsilon_\ell}$
73	32.2	1.73	0.0287	0.0044	0.00054	0.0252	2.79×10^{-10}
74	32.5	1.74	0.0288	0.0047	0.00069	0.0300	2.69×10^{-10}
74	32.6	1.74	0.0287	0.0052	0.0013	0.0512	3.32×10^{-10}
90	27.9	1.34	0.0411	0.0044	0.0024	0.0523	5.76×10^{-10}
91	28.1	1.35	0.0410	0.0048	0.0029	0.0596	5.21×10^{-10}
91	28.0	1.35	0.0410	0.0052	0.0049	0.0843	5.79×10^{-10}
106	24.8	1.11	0.0541	0.0044	0.010	0.1306	1.35×10^{-9}
107	24.8	1.10	0.0545	0.0048	0.012	0.1583	1.37×10^{-9}
107	24.8	1.10	0.0546	0.0053	0.016	0.1749	1.31×10^{-9}
133	21.0	0.84	0.0801	0.0047	0.087	0.5960	4.57×10^{-9}

TABLE 6.2. Averaged parameters and turbulence quantities for long-time simulations with different Re_λ. Approximately the same droplet size is used for all cases. Taken from Albernaz *et al.* (2016c).

An interesting behavior is observed for the temporal evolution of S^* when changing the Ohnesorge number and Re_λ. For $Re_\lambda \approx 74$, distinct peaks in S^* are present only for the higher Oh (lower surface tension). However, these peaks are seen for $Re_\lambda \approx 107$ independently of the Oh, as shown in Figure 6.9. The temporal behavior for different Ohnesorge numbers is not significantly different. This is reflected in the averaged quantities of S^* and We_d which show more substantial changes for lower Re_λ, as seen in Table 6.2. Figure 6.10 shows various deformed droplet shapes at different times, according to stars found in Fig. 6.9. The temperature distribution at the surface is also illustrated. The local equilibrium at the droplet surface shows low temperature regions associated with stronger curvature whereas higher temperature is obtained in flatter surface regions.
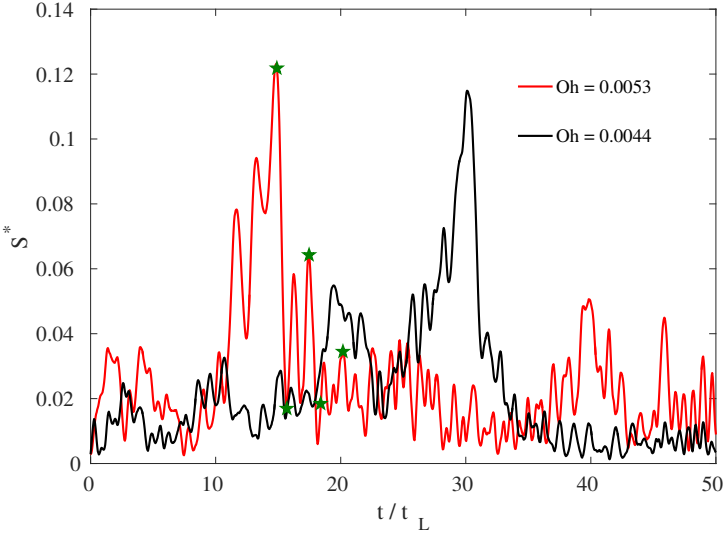

FIGURE 6.9. Deformation S^* evolution with time for $Re_\lambda \approx 107$. Taken from Albernaz *et al.* (2016c).
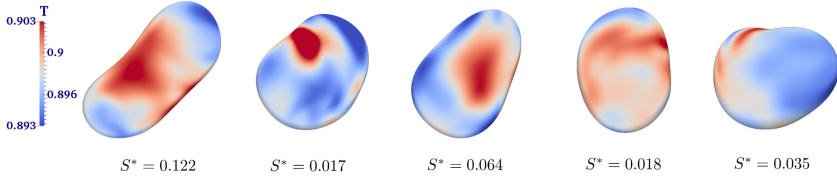

FIGURE 6.10. Temperature field at the droplet surface for different deformation values, for $Re_\lambda = 107$ and $Oh = 0.0053$. Taken from Albernaz *et al.* (2016c).

The oscillation frequency of the droplet has been investigated and compared to classical predictions by Rayleigh (1879). The basic modes of oscillation $n = 2$ and $n = 3$ could be identified for $Re_\lambda = 74$ (Fig. 6.11). However, for $Re_\lambda = 107$ as shown in Fig. 6.12, these modes are not distinct. Instead, they are replaced by a continuous spectrum, showing a decrease that scales as $\sim f^{-3}$.
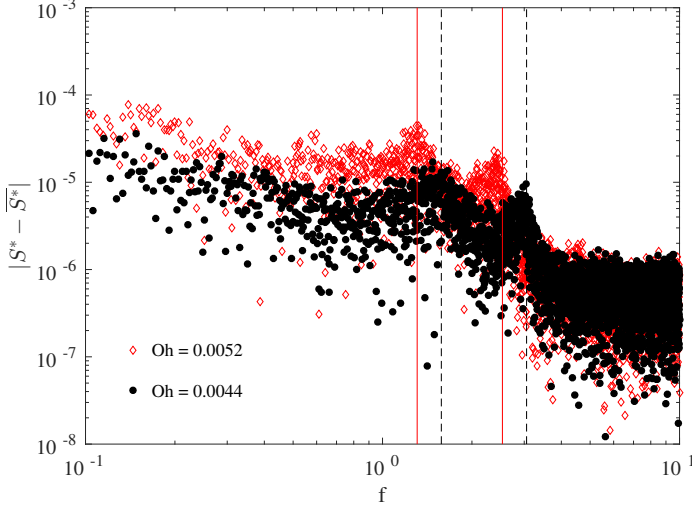

FIGURE 6.11. Power spectrum of the deformation parameter as a function of frequency for $Re_\lambda = 74$. The theoretical basic modes of oscillation are represented by solid lines ($Oh = 0.0052$) and dashed lines ($Oh = 0.0044$). Taken from Albernaz *et al.* (2016c).
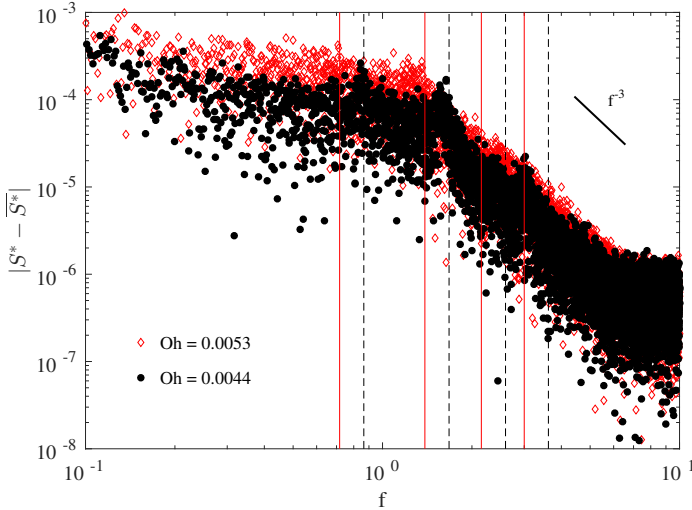

FIGURE 6.12. Power of the deformation parameter for $Re_\lambda = 107$, taken from Albernaz *et al.* (2016c).

Correlation coefficients have also been calculated, where We_d is strongly correlated with the liquid energy dissipation rate. A positive correlation is seen for the fluctuations of droplet volume and vapor temperature, which are more likely to happen between positive temperature fluctuation and droplet condensation, as shown in the joint probability distribution function in Figure 6.13. This result confirms that phase change is coupled to temperature fluctuations.
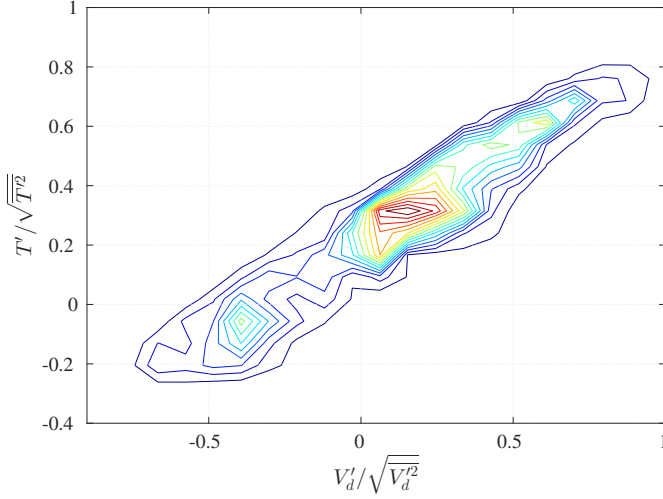

FIGURE 6.13. Contour lines for the joint p.d.f. of the temperature fluctuation in the domain T' with fluctuations of the droplet volume V_d', for $Re_\lambda = 74$. Taken from Albernaz et $al.$ (2016c).

CHAPTER 7

Concluding remarks

We have investigated the dynamics of an evaporative droplet under static conditions and forced convection. Unlike standard numerical approaches, where the interactions between different phases need to be described with appropriate jump conditions, we control the phase change directly by a non-ideal equation of state. This is possible by using a mesoscopic lattice Boltzmann method. We have first validated the evaporation rate and latent heat with a theoretical evaporation prediction, known as the D^2 law. An advantage of the absence of assumptions, such as constant surface tension forces and droplet temperature, resides in highlighting phenomena that are usually neglected, such as Marangoni forces. Under certain conditions, we have observed that the Marangoni effect plays a major role.

We have also used this model to study flows in isotropic turbulence. The novelty in using a non-ideal equation of state to establish local thermodynamic properties has led us to examine a single phase fluid approaching the critical point. Unreported phenomena have been revealed based on detailed analyses of thermodynamic variables behavior and different turbulent intensities. Lastly, we have investigated the dynamics of a droplet in turbulence. The heat and mass transfer, as well as the density contrast are considered. To the best of the authors' knowledge, such conditions have not been previously treated. Strong correlations between droplet deformation, volume fluctuations due to phase change occurrence and temperature fluctuations have been reported. We have also looked into the temporal spectra of droplet deformations coupled to the droplet oscillatory modes.

The main contribution of this work lies in the possibility of studying real fluids in both evaporative and turbulent environments. A spontaneous continuation of this work would be the inclusion of a multicomponent model. Instead of analyzing the droplet surrounded by its own vapor, the insertion of a gas would allow the study of other parameters such as the diffusion coefficient and mass fraction of different species. This improvement would bring the model closer to available experimental data, allowing its validation by a direct comparison.

Another suggestion for future work would be the investigation of droplet collisions surrounded by a gas with higher temperature. The primary focus would be on how phase change can affect droplet interactions. It would be interesting to consider a wide range of surface tension variation, which right now is a limitation to the present model: surface tension is not an independent

46

variable. Publications using lattice Boltzmann methods applied to multiphase flows have increased substantially over the last five years, where new models and approaches are opening doors to broaden applicability. A remedy to the surface tension might be found in a recent work by Xu *et al.* (2015), where surface tension can be tuned in order to assume a desirable value.

Further on, a similar model could also be used for simulating the breakup of a jet injected in a hot gas flow. As breakup is spontaneously included based on local thermal properties, several scales could be studied in detail without the use of modelling, as currently done by standard computational fluid dynamics. This would shed more light on how to optimize conditions for achieving homogeneity of the mixture of the fuel and the surrounding air. One would aim for a parameter investigation by changing properties such as surface tension and density ratio. The use of multicomponent models would allow investigations of the effect of additives in the fuel, with direct application to biodiesel fuels.

Acknowledgements

First of all I would like to express my gratitude to my supervisor Prof. Gustav Amberg. I am thankful for the opportunity of coming to Sweden, a country I learned to love, and for being his PhD student. It has been a pleasure working with Gustav, he always has something to contribute, either by insights or simply by motivation and positive attitude. Gustav is a kind person with a deep physical knowledge that spreads good energy independently of how well or bad things are. A big thanks to my co-supervisor Minh Do-Quang for his patience and for many fruitful discussions. Without his amazing knowledge in programming, this thesis would not have been possible.

I am grateful to my academic father and friend Prof. Francisco Ricardo (University of Brasilia) for his endless help and for sharing his passion for science. Thanks for introducing me to Fluid dynamics and all its different nuances. I would also like to acknowledge contributions to this work from Prof. Jim Hermanson (University of Washington).

Special thanks to my everyday office mates, former and actual ones: Yuli, Andreas, Zeinab, Amer, Timea and Abdul-Malik. I have to thank *los cabrones* for the good times we had and will surely keep having, Ricardo, Ramin, Pau, George, Werner, Sasan, Maffioli, Freddy, Walter, Jacopo, Prabal and Luis. *Jag tackar också all personal från avdelningen: ni har varit så hjälpsamma, särskilt Heide, Carolina, Malin och Bubba.*

Along this journey I am glad to have met so many people which made Mechanics such a nice environment, I would like to thank you all: Enrico, Stevin, Bernard, Karl, Lailai, Sohrab, Ferro, Azad, Lukas, Matteo, Alex, Yuki, Alexandra, Ashwin, Geert, Elektra, Tomas, Shervin, Ugis, Nima, Iman, Armin, Erik, Priti, Ekaterina, Jiewei, Mehdi, Mireia, Igor, Emanuele, Mattias, Nicolas, Taras, Brandt, Biancofore, Gaetano, Picano and others which I might have forgotten to include. That's what happens when you leave this part to be written last.

And talking about last, but not least, my deepest gratitude to my family. Mamadinha and Vanessa, you have always been there, encouraging and supporting me. *Sou eternamente grato!* I have so much luck in my life for having you and for having my *sambo* Fannie: *tack älskling för ditt stöd och för all kärlek som du ger mig: du är min glädje!*

Bibliography

ALBERNAZ, D. L., DO-QUANG, M. & AMBERG, G. 2013 Lattice boltzmann method for the evaporation of a suspended droplet. *Interfac. Phenom. Heat Transfer* **1**, 245–258.

ALBERNAZ, D. L., DO-QUANG, M. & AMBERG, G. 2015 Multirelaxation-time lattice boltzmann model for droplet heating and evaporation under forced convection. *Phys. Rev. E* **91**, 043012.

ALBERNAZ, D. L., AMBERG, G. & DO-QUANG, M. 2016a Simulation of a suspended droplet under evaporation with Marangoni effects. *accepted for publication in Int. J. Heat Mass Transf*.

ALBERNAZ, D. L., DO-QUANG, M., HERMANSON, J. C. & AMBERG, G. 2016b Real fluids near the critical point in isotropic turbulence. *under revision in Phys. Fluids*.

ALBERNAZ, D. L., DO-QUANG, M., HERMANSON, J. C. & AMBERG, G. 2016c Droplet deformation and heat transfer in isotropic turbulence. *submitted to J. Fluid Mech.*.

BALAJI, B. RAGHAVAN, V., RAMAMURTHI, & GOGOS, K.G. 2011 A numerical study of evaporation characteristics of spherical n-dodecane droplets in high pressure nitrogen environment. *Phys. Fluids* **23**, 063601.

BANERJEE,R. 2013 Numerical investigation of evaporation of a single ethanol/iso-octane droplet. *Fuel* **107**, 724–739.

BIRD, R. B. 1960 *Transport Phenomena*. John Wiley & Sons, New York.

BHATNAGAR, P. L., GROSS, E. P. & KROOK, M. 1954 Model for collision processes in gases. *Phys. Rev.* **94**, 511–525.

BORG, A., BOLINDER J. & FUCHS, L. 2001 Simultaneous velocity and concentration measurements in the near-field of a turbulent low-pressure jet by DPIV-PLIF region of a turbulent jet flow. *Exp. in Fluids* **31**, 140–152.

CHEN, S. & DOOLEN, G. D. 1998 Lattice boltzmann method for fluid flows. *Annu. Rev. Fluid Mech.* **30**, 329–364.

CHIN, J. 2001 *Mesoscale modelling with the Lattice Boltzmann Method*. University of London.

DEC, J. E. 1997 A conceptual model of DI diesel combustion based on laser-sheet imaging. *SAE Paper*, 970873.

DONZIS, D. A. & JAGANNATHAN, S. 2013 Fluctuations of thermodynamic variables in stationary compressible turbulence. *J. Fluid Mech.* **733**, 221–244.

ERBIL, H. Y. 2012 Evaporation of pure liquid sessile and spherical suspended drops: A review. *Adv. Colloid Interface Sci.* **170**, 67–86.

FAGHRI, A. & ZHANG, Y. 2006 *Transport phenomena in multiphase systems.* Elsevier, Oxford.

GAN, Y., XU, A., ZHANG, G., ZHANG, P. & LI, Y. 2012 Lattice boltzmann study of thermal phase separation: Effects of heat conduction, viscosity and prandtl number. *EPL* **97**, 44002.

GONNELLA, G., LAMURA, A. & SOFONEA, V. 2007 Lattice boltzmann simulation of thermal nonideal fluids. *Phys. Rev. E* **76**, 036703.

GOROKHOVSKI, M. & HERRMANN, M. 2007 Modelling Primary Atomization. *Annu. Rev. Fluid Mech.* **40**, 343–366.

GOTOH, T. & FUKAYAMA, D. 2001 Pressure spectrum in homogeneous turbulence. *Phys. Rev. Lett.* **86**, 1775–3778.

GRIGORIEV, I. G., WALLIN, S. W., BRETHOUWER, G. B. & JOHANSSON, A. V. J. 2013 A realizable explicit algebraic Reynolds stress model for compressible turbulent flow with significant mean dilatation. *Phys. Fluids* **25**, 105112.

GUILLARD, F., FRITZON, R., REVSTEDT, J., TRÄGARDH, C., ALDEN, M. & FUCHS, L. 1998 Mixing in a confined turbulent impinging jet using planar laser induced fluorescence. *Exp. in Fluids* **25**, 143–150.

GUYON, E., HULIN, J.-P., PETIT, L. & MITESCU, C. D. 2001 *Physical hydrodynamics.* University Press, Oxford.

HASE, M. & WEIGAND, B. 2004 Transient heat transfer of deforming droplets at high reynolds numbers. *Int. J. Numer. Methods Heat Fluid Flow* **14**, 85–97.

HE, X. & DOOLEN, G. D. 2002 Thermodynamic foundations of kinetic theory and lat- tice Boltzmann models for multiphase flows. *J. Stat. Phys.* **107**, 309–328.

HOLYST, R., LITNIEWSKI, M., JAKUBCZYK, D., KOLWAS, K. & KOLWAS, M. 2013 Evaporation of freely suspended single droplets: experimental, theoretical and computational simulations. *Rep. Prog. Phys.* **76**, 034601.

ISHIHARA, T., GOTOH, T. & KANEDA, Y. 2009 Study of high–reynolds number isotropic turbulence by direct numerical simulation. *Annu. Rev. Fluid Mech.* **41**, 165–180.

JIANG, S., SIAMAS, G. A., JAGUS, K. & KARAYIANNIS, T. G. 2010 Physical modelling and advanced simulations of gas-liquid two-phase jet flows in atomization and sprays. *Progress in Energy and Combustion Science* **36**, 131–167.

KAPLUN, A.B. & MESHALKIN, A.B. 2003 Thermodynamic validation of the form of unified equation of state for liquid and gas, *High Temperature* **41**, 319-326.

KÉKESI, T., GUSTAV, A. & WITTBERG, L. P. 2014 Drop deformation and breakup. *Int. J. Multiphase Flow* **66**, 1–10.

KIDA, S. & ORZAG, S. A. 1990 Energy and spectral dynamics in forced compressible turbulence. *J. Sci. Comput.* **5**, 85–125.

KOLMOGOROV, A. N. 1994a The local structure of turbulence in incompressible viscous fluid for very large Reynolds numbers [In Russian]. *Dokl. Akad. Nauk SSSR* **30**, 299–301.

KOLMOGOROV, A. N. 1994b Dissipation of energy in locally isotropic turbulence [In Russian]. *Dokl. Akad. Nauk SSSR* **32**, 19–21.

Kuo, K. K. Y. 2005 *Principles of Combustion.* John Wiley & Sons, New York.

Kupershtokh, A. L. & Medvedev, D. A. 2006 Lattice boltzmann equation method in electrohydrodynamic problems. *J. Electrostat.* **64**, 581–585.

Kupershtokh, A. L., Medvedev, D. A. & Karpov, D. I. 2009 On equations of state in a lattice boltzmann method. *Comput. Math. Appl.* **58**, 965–974.

Lallemand, P. & Luo, L. S. 2000 Theory of the lattice boltzmann method: Dispersion, dissipation, isotropy, galilean invariance, and stability. *Phys. Rev. E* **61**, 6546.

Lasheras, J. C., Villermaux, E. & Hopfinger, E. J. 1998 Break-up and atomization of a round water jet by a high-speed annular air jet. *J. Fluid. Mech.* **357**, 351–379.

Lefebvre, A. H. 1989 *Atomization and sprays.* Taylor & Francis, Bristol.

Levich, V. G. 1962 *Physicochemical hydrodynamics.* Englewood Cliffs, N.J.: Prentice-Hall.

Marangoni, C. G. M. 1871 Ueber die ausbreitung der tropfen einer flüssigkeit auf der oberflache einer anderen. *Ann. Phys. Chem.* **143**, 337–354.

Márkus, A. & Házi, G. 2011 Simulation of evaporation by an extension of the pseudopotential lattice boltzmann method: A quantitative analysis. *Phys. Rev. E* **83**, 046705.

Lemmon, E.W., McLinden, M.O. & Friend, D.G. 2013 Thermophysical Properties of Fluid Systems. In *NIST Chemistry WebBook, NIST Standard Reference Database Number* (ed. Linstrom P.J. & Mallard W.G.), vol. 69. National Institute of Standards and Technology, Gaithersburg MD.

Perlekar, P., Biferale, L., Sbragaglia, M., Srivstava, S. & Toschi, F. 2012 Droplet size distribution in homogeneous isotropic turbulence. *Phys. Fluids* **24**, 065101.

Pope, S. B. 2000 *Turbulent flows.* Cambridge University Press, Cambridge.

Probstein, R. F. 1994 *Physicochemical hydrodynamics: an introduction.* John Wiley & Sons, New York.

Pumir, A. 1994 A numerical study of pressure fluctuations in three-dimensional, incompressible, homogeneous, isotropic turbulence. *Phys. Fluids* **6**, 2071–2083.

Qian, D., McLaughlin, J. B., Sankaranarayanan, K., Sundaresan, S. & Kontomaris, K. 2006 Simulation of bubble breakup dynamics in homogeneous turbulence. *Chem. Eng. Comm.* **193**, 1038–1063.

Reynolds, O. 1895 On the dynamical theory of incompressible viscous fluids and the determination of the criterion. *Philos. Trans. Roy. Soc. London* **186**, 123–164.

Rayleigh, Lord 1879 On the capillary phenomena of jets. *Proc. R. Soc. London* **29**, 71–97.

Rayleigh, Lord 1883 Investigation of the character of the equilibrium of an incompressible heavy fluid of variable density. *Proc. London Math. Soc.* **14**, 170–177.

Richardson, L. F. 1922 *Weather Prediction by Numerical Process.* Dover Publications, Inc., New York.

Safari, H., Rahimian, M. H. & Krafczyk, M. 2013 Extended lattice boltzmann method for numerical simulation of thermal phase change in two-phase fluid flow. *Phys. Rev. E* **88**, 013304.

SAZHIN, S. S. 2006 Advanced models of fuel droplet heating and evaporation. *Prog. Energy Combust. Sci.* **32**, 162–214.

SBRAGAGLIA, M., BENZI, R., BIFERALE, L., CHEN, H., SHAN, X. & SUCCI, S. 2009 Lattice boltzmann method with self-consistent thermo-hydrodynamic equilibria. *J. Fluid Mech.* **628**, 299–309.

SCARDOVELLI, R. & ZALESKI, S. 1999 Direct numerical simulation of free-surface and interfacial flow. *Annu. Rev. Fluid Mech.* **31**, 567–603.

SCHLOTTKE, J. & WEIGAND, B. 2008 Direct numerical simulation of evaporating droplets. *J. Comput. Phys.* **227**, 5215–5237.

SEDARSKY, D., BERROCAL, E. & LINNE, M. 2008 Ballistic imaging for measurement of flow structures in dense multiphase media. 14th *International Symposium on Applications of Laser Techniques to Fluid Mechanics*.

SETHIAN, J. A. & SMEREKA, P. 2003 Level set methods for fluid interfaces. *Annu. Rev. Fluid Mech.* **35**, 341–372.

SHAN, X. & CHEN, H. 1993 Lattice boltzmann model for simulating flows with multiple phases and components. *Phys. Rev. E* **47**, 1815.

SHAN, X. & CHEN, H. 1994 Simulation of nonideal gases and liquid-gas phase transitions by the lattice Boltzmann equation. *Phys. Rev. E* **49**, 2941.

SHAN, X., YUAN, X. F. & CHEN, H. 2006 Kinetic theory representation of hydrodynamics: a way beyond navier-stokes equation. *J. Fluid Mech.* **550**, 413–441.

SHI, Y., GE, H.-W. & REITZ, R. D. 2011 *Computational Optimization of Internal Combustion Engines.* Springer-Verlag, London.

SHINJO, J. & UMEMURA, A. 2010 Simulation of liquid jet primary breakup: Dynamics of ligament and droplet formation. *Int. J. Multiphase Flow* **36**, 513–532.

SHINJO, J. & UMEMURA, A. 2011 Detailed simulation of primary atomization mechanisms in Diesel jet sprays (isolated identification of liquid jet tip effects) *Proc. Combust. Inst.* **33**, 2089–2097.

SIRIGNANO, W. A. 2010 *Fluid Dynamics and Transport of Droplets and Sprays.* Cambridge University Press, Cambridge.

STROTOS, G., GAVAISES, M., THEODORAKAKOS, A. & BERGELES, G. 2011 Numerical investigation of the evaporation of two-component droplets. *Fuel* **90**, 1492–1507.

SUKOP, M.C. & THORNE, D.T. 2006 *Lattice Boltzmann modelling: an introduction for geoscientists and engineers.* Berlin: Springer.

TAYLOR, C. F. 1985 *The internal-combustion engine in theory and practice.* MIT Press, Cambridge.

TANGUY, S., MENARD, T. & BERLEMONT, A. 2007 A level set method for vaporizing two-phase flows. *J. Comput. Phys.* **221**, 837–853.

TRYGGVASON, G., BRUNNER, B., ESMAEELI, A., JURIC, D., AL-RAWAHI, N., TAUBER, W., HAN, J., NAS, S. & JAN, Y.-J. 2001 A front-tracking method for the computations of multiphase flow. *J. Comput. Phys.* **169**, 708–759.

TSUJI, Y. & ISHIHARA, T. 2003 Similarity scaling of pressure fluctuation in turbulence. *Phys. Rev. E* **68**, 026309.

WAGNER, A. J. & YEOMAS, J. M. 1999 Phase separation under shear in two-dimensional binary fluids. *Phys. Rev. E* **59**, 4366–4373.

XU, A., TAO, T. S., AN, L. & SHI, L. 2015 A three-dimensional pseudo-potential-based lattice Boltzmann model for multiphase flows with large density ratio and variable surface tension. *Int. J. Heat Fluid Flow* **56**, 261–271.

P. YUAN, & SCHAEFER, L. 2006 Equations of state in a lattice Boltzmann model, *Phys. Fluids* **18**, 042101.

ZHANG, H. 2003 Evaporation of a suspended droplet in forced convective high-pressure environments. *Combust Sci. and Tech.* **175**, 2237–2268.

ZHANG, R. & CHEN, H. 2003 Lattice boltzmann method for simulations of liquid-vapor thermal flows. *Phys. Rev. E* **67**, 066711.